

A Multilayered Block Network Model to Forecast Large Dynamic Transportation Graphs: an Application to US Air Transport

Hector Rodriguez-Deniz^{a,*}, Mattias Villani^{a,b}, Augusto Voltes-Dorta^c

^a*Division of Statistics and Machine Learning, Linköping University, Sweden*

^b*Department of Statistics, Stockholm University, Sweden*

^c*Management Science and Business Economics Group, University of Edinburgh, United Kingdom*

Abstract

Dynamic transportation networks have been analyzed for years by means of static graph-based indicators in order to study the temporal evolution of relevant network components, and to reveal complex dependencies that would not be easily detected by a direct inspection of the data. This paper presents a state-of-the-art probabilistic latent network model to forecast multilayer dynamic graphs that are increasingly common in transportation and proposes a community-based extension to reduce the computational burden. Flexible time series analysis is obtained by modeling the probability of edges between vertices through latent Gaussian processes. The models and Bayesian inference are illustrated on a sample of 10-year data from four major airlines within the US air transportation system. Results show how the estimated latent parameters from the models are related to the airline's connectivity dynamics, and their ability to project the multilayer graph into the future for out-of-sample full network forecasts, while stochastic blockmodeling allows for the identification of relevant communities. Reliable network predictions would allow policy-makers to better understand the dynamics of the transport system, and help in their planning on e.g. route development, or the deployment of new regulations.

Keywords: transportation networks, multilayer graphs, air transport, machine learning

1. Introduction and related work

We live in a highly interconnected world, and networks have become an integral part of our life, from telecommunications and social media to transportation systems and the Internet of Things. Further technological advances and the advent of automation, which may enable the autonomous operation of actors within the network, are likely to push the scale and sophistication of network systems up to new levels in the near future. This increasing complexity has permeated into science in a natural way, and the use of network modeling has become widespread in disciplines as diverse as Sociology, Neuroscience or Transportation (Jasny et al., 2009; Barabási, 2016), propelled by the availability of data and computing power. Transportation science has been for many decades an active field aiming for the development of models and policies that ensure the efficiency, safety and social acceptability of transportation systems, while limiting costs and environmental impact. In recent years there has been a growing number of research directions that reveal the need for appropriate methods to address the complexity imposed by network problems. Network resilience analysis against e.g. natural disasters or terrorist attacks, structural evolution of network systems, and network-wide traffic forecasting, are examples of these new directions. The interest in modeling and understanding transportation networks is not merely academic. The maritime shipping network processes over 80% of the world

*Corresponding author

Email addresses: hector.rodriguez@liu.se (Hector Rodriguez-Deniz), mattias.villani@stat.su.se (Mattias Villani), augusto.voltes-dorta@ed-ac.uk (Augusto Voltes-Dorta)

trade, whereas travel and tourism industries, which sustain 10% of the global GDP, rely on the air transport network (UNCTAD, 2017; WTTC, 2018). Also, public transport networks are a key element in the infrastructure of large urban areas, where the bulk of the economic activity is concentrated in most developed countries.

Here we focus on multilayer dynamic networks and use latent variable models for analyzing complex graph data that are increasingly available in transportation and related fields. Multilayer networks add a new dimension to the network representation through the definition of layers, and allow for the modeling of complex systems that would be difficult to represent using regular, "flat" graphs. Multilayer networks can be defined and structured in various ways depending on the problem and the specific role of the layers (Kivelä et al., 2014). In transportation, a multilayer graph could represent how different airlines interact with the underlying airport network, or how different transport modes (e.g. bus and metro networks) operate simultaneously within a public transportation system. Dynamic networks, on the other hand, add a temporal dimension to the problem by assuming that the interaction between the elements in the network change over time, which is common in transport systems, as discussed below. A latent network model (Kolaczyk, 2017; Crane, 2018) is a probabilistic model that uses unobserved features to characterize different properties and processes within a graph. These models are flexible and allow for e.g. link prediction and community detection, and are also relatively easy to estimate, see Section 2 for further details and relevant literature.

Dynamic transportation networks have been studied for years, both from short-term and long-term perspectives. Studies featuring a long-term approach usually aim to analyze the structural dynamics of the transportation system in order to assess the temporal evolution of relevant network components in terms of months or years, and to reveal complex dependencies and patterns that would not be easily detected by a direct inspection of the data. A graph-based analysis through the use of measures such as e.g. the node degree or betweenness (Guimera et al., 2005) became the *de facto* methodological approach, which has been also used to study the dynamics of shipping and airport networks (Ducruet and Notteboom, 2012; Wang et al., 2014), or airline de-hubbing (Rodríguez-Déniz et al., 2013), among many others. On the other hand, short-term network dynamic problems usually deal with time spans of minutes or hours, and focus on modeling specific elements within the network (e.g. link congestion) rather than adopting a structural approach. A good example of a short-term network problem in transportation is urban traffic forecasting. This is a time-series prediction problem that has been traditionally addressed with statistical and machine learning models (Vlahogianni et al., 2014), and where an explicit graph-based representation of the network is not strictly necessary. We believe there is an opportunity for a methodological advance in studies involving the long-term analysis of transportation networks by using state-of-the-art statistical models for dynamic and multilayer graph data, therefore moving from the current descriptive, indicator-based approach to an inferential one. Moreover, reliable graph forecasting would allow for the definition of benchmarking scenarios in problems where origin-destination pairs are usually assumed fixed. Examples of those applications would be airline schedule optimization (Cadarsó and de Celis, 2017), cargo assignment in shipping networks (Wang et al., 2016) and hub-location (Alkaabneh et al., 2019), to name a few.

In spite of the above, there have been some recent contributions to model-based inference in transportation graphs. A representative example is the paper from Kotegawa et al. (2010), which addresses the problem of route (link) prediction in air transportation networks. Their work is motivated by the air traffic forecasts from the US Federal Aviation Administration (FAA), which does not consider network dynamics in their predictions. The authors tackle the graph forecasting problem by training a model that uses topological characteristics of the airports as covariates, and yield the probability of city-pairs being connected by new routes in the future. Three competing models (logistics regression, neural networks, and a preferential attachment algorithm) were tested, with the artificial neural network being the top performer. The authors stress that given the competitive nature of the airline industry and its implications on the network's structure (e.g. dehubbing), reliable network forecasts would allow policy-makers to better understand the dynamics of the system, and help in their planning on e.g. infrastructure development, or the deployment of new regulations. Similarly, de Wit and Zuidberg (2016) perform an econometric analysis to study the probability of market closures for

European low-cost carriers. They implement a logistic regression model with route-based covariates (e.g. distance, offered seats) that could help identify the factors that make markets more likely to be canceled, although their approach lack the network and dynamic perspective.

Working with large graphs can be computationally tough, and transportation networks are no exception to that. A practical way to circumvent this issue that has been recently adopted in the literature is to reduce the scale of the problem by partitioning the graph. In graph clustering, also known as community detection (see e.g. Fortunato, 2010) or stochastic blockmodeling (Nowicki and Snijders, 2001; Airoldi et al., 2008), the objective is to find groups of highly interconnected elements within the network, which may reveal structures such as e.g. social cliques or spatial patterns. In a public transport context, Yap et al. (2019) used a two-pronged strategy to reduce the size of their transfer synchronization problem. First they performed spatial clustering to isolate relevant transfer locations, and then used graph-based community detection to determine which line bundles within the selected hubs to synchronize. Tian et al. (2020) greatly reduced the computational cost in a large-scale rebalancing problem by clustering their bike-sharing network into five management areas. Still, graph clustering has not been exclusively used to deal with the computational bottleneck. Yildirimoglu and Kim (2018) use modularity-based community detection to find demand patterns in an urban multilayer setting (bus, passenger and car networks), thus allowing for a demand analysis at different spatial resolutions that may be helpful for planning and operation, whereas Olmos et al. (2020) identified relevant demand clusters for a better design of a network of bicycle paths. One aspect that is common among the previous studies is that the clustering is framed as a separate spatial problem, without explicitly considering the dynamics of the network.

The aim of this paper is threefold: i) present a state-of-the-art latent network model to forecast multilayer dynamic graphs that are increasingly common in transportation, which have potential applications to the long-term analysis of transportation networks, ii) propose a community-based extension of the model to reduce the computational burden by jointly considering the temporal and spatial dimensions of the network, and iii) demonstrate their applicability to a real multilayer transportation network in two case studies with US airline data.

The rest of the manuscript is organized as follows. Section 2 briefly introduce relevant work on statistical models for network data. The methodological framework and the community-based model are detailed in Section 3, whereas in Section 4 a set of validation experiments are performed. Section 5 presents applications to real data from an airline network. The last section summarizes the paper and discuss limitations and possible directions for further research.

2. Statistical models for graph data

Statistical network analysis is a well-established field of research (see e.g. Kolaczyk, 2009) with origins dating back to the seminal work on random graphs by Erdős and Renyi (1959). Despite their fundamental contributions, the original mathematical models, along with other recent models such as the “small-worlds” from Watts and Strogatz (1998) and the hub-and-spoke networks from Barabási and Albert (1999), are too limited for most applications. Exponential Random Graph Models (ERGMs) were designed with this aim in mind, initially with the p_1 model from Holland and Leinhardt (1981), and define an exponential family of distributions over a graph. However, model degeneracy and intractability are still unresolved problems, which has represented a hurdle for a wider applicability outside social networks. Interestingly, Zhang et al. (2019) recently used ERGM models to learn social networks effects that can be used to generate synthetic populations in agent-based transport simulators.

In contrast with the log-linear approach of the ERGMs, latent network models (LNMs) define latent classes or features to capture the network complexity in a non-linear fashion. The Stochastic Block Model (SBM - Holland et al., 1983) is perhaps the most popular latent network model, and assumes a latent community structure that drives the relationship patterns between actors in the network. Nowicki and Snijders (2001) proposed a Bayesian inference algorithm using Gibbs sampling whereas Daudin et al. (2008) developed variational inference for the model. Current research on SBM’s is mainly aimed at mixed membership clustering (Airoldi et al., 2008), extensions for weighted graphs

(Aicher et al., 2014), dynamic and state-space modeling (Ishiguro et al., 2010; Xu and Hero, 2014), and multi-layer networks (Han et al., 2015; Stanley et al., 2016). A different approach to LNMs is to define a latent space over the network nodes themselves (Hoff et al., 2002). In this case, the probability that two network elements are connected can be defined in terms of a distance function, in such a way that nodes neighboring in the unobserved latent space are more likely to be connected. Latent space models are able to capture transitive dependencies in a natural way (in contrast with SBM’s) and are flexible enough to incorporate dynamics while allowing for practical maximum likelihood and Bayesian inference. More recently, Durante and Dunson (2014) introduce exact Bayesian inference using Pólya-Gamma augmentation (Polson et al., 2013) for a dynamic latent space network model driven by Gaussian Processes. A natural extension of the previous model to a dynamic multilayer setting is presented in Durante et al. (2017), although scalability issues arise for large network data since the model introduces a Gaussian process for each node in each layer.

3. Methodology

3.1. Dynamic Multilayered Network Model

We first describe the dynamic multilayered network model in Durante and Dunson (2014) and Durante et al. (2017) that serves as a starting point for our community-based extension. We represent a network as a graph $G = (V, E)$ where V is the set of vertices (also called nodes) $i = 1, \dots, N$ and E a set of unweighted edges (also called links) between node pairs $\{i, j\}$. The connectivity of the graph is summarized in the $N \times N$ adjacency matrix A_{ij} , where $A_{ij} = 1$ if there is an edge connecting vertices i and j , and $A_{ij} = 0$ otherwise. We assume undirected edges and no self-loops, i.e. $A_{ij} = A_{ji}$ and $A_{ii} = 0$. Dynamic multilayer graphs have a graph per layer that evolves in time and can be represented by adjacency matrices $A_{ij}^k(t)$ where $A_{ij}^k(t) = 1$ if vertices i and j are connected in layer $k = 1, \dots, K$ at time $t = t_1, \dots, t_T$.

The dynamic multilayer network model in Durante and Dunson (2014) and Durante et al. (2017) defines a Bayesian logistic regression for each element in the adjacency matrix $A_{ij}^k(t)$, i.e. for each possible edge in the graph at any layer k and time t . The logit of the probability that any two vertices in the multilayer graph are connected depends on a model with three additive components featuring unobserved variables that encode connectivity patterns. Specifically, the model is of the form

$$A_{ij}^k(t) \sim \text{Bernoulli}(\pi_{ij}^k(t))$$

$$\psi_{ij}^k(t) = \text{Logit}(\pi_{ij}^k(t)) = \mu(t) + \sum_{r=1}^R \bar{x}_{ir}(t)\bar{x}_{jr}(t) + \sum_{h=1}^H x_{ih}^k(t)x_{jh}^k(t), \quad (1)$$

where the latent processes, $\mu(t)$, $\bar{x}_{ir}(t)$ and $x_{ih}^k(t)$, are assumed to be smoothly evolving Gaussian processes with RBF kernel functions (Rasmussen and Williams, 2006)

$$\mu(t) \sim \mathcal{GP}(0, k_\mu) \quad (2a)$$

$$\bar{x}_{ir}(t) \sim \mathcal{GP}(0, \tau_r^{-1}k_{\bar{x}}) \quad (2b)$$

$$x_{ih}^k(t) \sim \mathcal{GP}(0, \tau_h^{k-1}k_x). \quad (2c)$$

The model is structured through a set of latent variables that capture different effects within the network. The global time-varying intercept $\mu(t)$ defines a baseline network density for all nodes in all layers. The cross-layer effects $\bar{x}_i(t)$ enter as a bilinear form (Hoff, 2005), increasing the probability of a link between vertices as their latent coordinates become aligned whereas the within-layer $x_i^k(t)$ coordinates act in an identical manner capturing those effects not shared across the different layers. Instead of learning the dimensionality R and H of the latent coordinates $\bar{x}_{ir}(t)$, $r = 1, \dots, R$ and

$x_{ih}^k(t), h = 1, \dots, H$, the model uses multiplicative inverse Gamma priors (Bhattacharya and Dunson, 2011) to induce a shrinkage effect that becomes stronger for larger r and h

$$\tau_r^{-1} = \prod_{u=1}^r \delta_u^{-1}, \quad r = 1, \dots, R \quad (3)$$

$$\delta_1 \sim \text{Gamma}(a_1, 1), \quad \delta_{u>1} \sim \text{Gamma}(a_2, 1) \quad (4)$$

$$(\tau_h^k)^{-1} = \prod_{v=1}^h (\delta_v^k)^{-1}, \quad h = 1, \dots, H, \quad k = 1, \dots, K \quad (5)$$

$$\delta_1^k \sim \text{Gamma}(a_1, 1), \quad \delta_{v>1}^k \sim \text{Gamma}(a_2, 1). \quad (6)$$

Durante et al. (2017) prove that the model in Eq.(1) is very flexible and can essentially model any matrix of edge probabilities if R and H is large enough. The likelihood factorizes into a set of Bernoulli logistic regressions which can be Gibbs sampled using the Pólya-Gamma data augmentation in Polson et al. (2013). However, the number of Gaussian processes that needs to be learned from data is $1 + RN + HKN$, which makes computations and storage unmanageable for anything except small networks with few layers and small number of nodes. Moreover, the model is completely unstructured and is therefore massively overparametrized when the data follow some structure, e.g. some sort of community clustering. In the next section we propose a SBM extension of the model with a dramatically reduced number of Gaussian processes and develop a Gibbs sampling algorithm for inference using the Pólya-Gamma data augmentation trick. The model imposes a community structure and is therefore less general than Durante et al. (2017), but benefits from a reduction in the number of Gaussian processes and scales much better to larger networks.

3.2. Dynamic Multilayered Block Network Model

To impose a community structure we assume that each vertex in the network belongs to a stochastic block (Nowicki and Snijders, 2001) or cluster $b \in \{1, \dots, B\}$ with prior probability $p(z_i = b) = \eta_b$, where z is the vector of block assignments, indicating to which block each vertex i belongs, and $\eta \sim \text{Dirichlet}(\alpha_1, \dots, \alpha_B)$. This results in logistic regressions that model the interactions between groups of vertices, i.e. the probability of the existence of an edge between any two vertices in the network now depends on which block/cluster they belong. We propose the following block model extension of Durante et al. (2017)

$$z_i \sim \text{Categorical}(\eta_1, \dots, \eta_B)$$

$$A_{ij}^k(t) | (z_i = p, z_j = q) \sim \text{Bernoulli}(\pi_{pq}^k(t)) \quad (7)$$

$$\psi_{pq}^k(t) = \text{Logit}(\pi_{pq}^k(t)) = \begin{cases} \mu(t) + \sum_{r=1}^R \bar{x}_{pr}(t) \bar{x}_{qr}(t) + \sum_{h=1}^H x_{ph}^k(t) x_{qh}^k(t) & \text{if } p \neq q \\ \mu_p^k(t) + \sum_{r=1}^R \bar{x}_{pr}(t) & \text{if } p = q \end{cases} \quad (8)$$

The link probabilities $\pi_{pq}^k(t)$ for $p \neq q$ are of the same form as in Durante et al. (2017), but here defined over blocks, for a given block assignment. The within-block link probabilities for $p = q$ are modeled separately with a dynamic intercept per block and layer $\mu_p^k(t)$, and a second term with the sum of cross-layer coordinates of the corresponding block that allows for some block-wise leveraging between the two logits. See Figure 1 for a graphical representation.

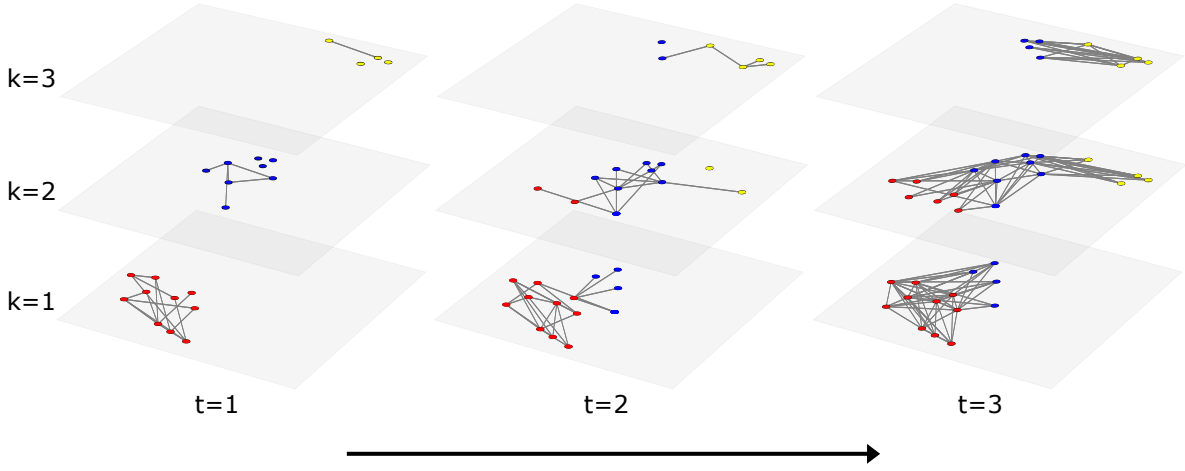


Figure 1: Example of a dynamic multilayer network with three stochastic blocks (red, blue and yellow), layers and time points.

3.3. A Scalable Gibbs Sampler for Bayesian Inference

The complete-data likelihood for the proposed model is

$$p(A_{ij}^k(t)|\psi_{pq}^k(t)) = \prod_{t=1}^T \prod_{k=1}^K \prod_{i=2}^N \prod_{j=1}^{i-1} \frac{\exp(\psi_{z_i z_j}^k(t))^{A_{ij}^k(t)}}{1 + \exp(\psi_{z_i z_j}^k(t))} = \prod_{t=1}^T \prod_{k=1}^K \prod_{p=1}^B \prod_{q=1}^p \frac{\exp(\psi_{pq}^k(t))^{y_{pq}^k(t)}}{[1 + \exp(\psi_{pq}^k(t))]^{n_{pq}^k(t)}},$$

where $\psi_{pq}^k(t) = \text{Logit}(\pi_{pq}^k(t))$, and $n_{pq}^k(t)$ and $y_{pq}^k(t)$ are the number of possible and actual edges in $A_{ij}^k(t)$ between blocks p and q , respectively. The block model induces a set of within-block summations over edges that structures the likelihood into TK explicit Binomial components instead of the Bernoulli components in Durante et al. (2017). This likelihood allows for exact Bayesian inference using Gibbs sampling with the Pólya-Gamma data augmentation for Binomial logistic regression in Polson et al. (2013), while automatically reducing the model size for large network problems as the estimation will be over $B(B+1)/2$ blocks instead of $N(N-1)/2$ vertices, where $B \ll N$.

In Appendix B.1 we briefly review the Pólya-Gamma data augmentation method (Polson et al., 2013), which provides a tractable, efficient way to perform Bayesian inference on models with binomial likelihoods, whereas Appendix B.2 gives a detailed description of a Gibbs sampler algorithm to sample from the joint posterior of all model parameters. The sampler combines the multilayer network model from Durante et al. (2017), modified to our specific structure of the block link probabilities in Eq.(8), with updating steps for the latent block allocations \mathbf{z} and block probabilities $\boldsymbol{\eta}$ following Nowicki and Snijders (2001).

The Gibbs sampler in Durante et al. (2017) involves $TKN(N-1)/2$ draws from the $\text{PG}(1, c)$ distribution. Appendix B.2 shows that this step in our algorithm includes $TKB(B+1)/2$ updating step for the Pólya-Gamma variables $\omega_{pq}^k(t) \sim \text{PG}(b, c)$, where $b = n_{pq}^k(t)$. Hence, although the number of draws is dramatically smaller for our algorithm, each draw tends to be more costly since the time to simulate from $\text{PG}(b, c)$ increase in b . To speed up computations we follow up on the suggestion mentioned in Windle et al. (2014) and develop a fast normal approximation via moment-matching; see Appendix A. Figure 2 (left) show the mean absolute error between the normal approximation and the sampling methods from (Devroye, 2009; Polson et al., 2013), relative to the theoretical mean. We see that for values of $b \geq 50$ the deviation from the theoretical mean is less than 20% in the worst case where $c < 10$ and negligible for $c \geq 10$. Simulation times are independent from b when sampling

Model	B	R	H	l_μ	l_{μ_p}	$l_{\bar{x}}$	l_x	a_1	a_2	MCMC Samples
DMN	-	6	6	0.05	-	0.05	0.05	2	2	5,000 (20% burnin)
DMBN	10	6	6	0.05	0.05	0.05	0.05	2	2	5,000 (20% burnin)

Table 1: Parameter configuration of the two models for the experiment

from the approximation (right). Therefore, we use our normal approximation to sample Pólya-Gamma variables for $b \geq 100$, and the standard exact methods otherwise.

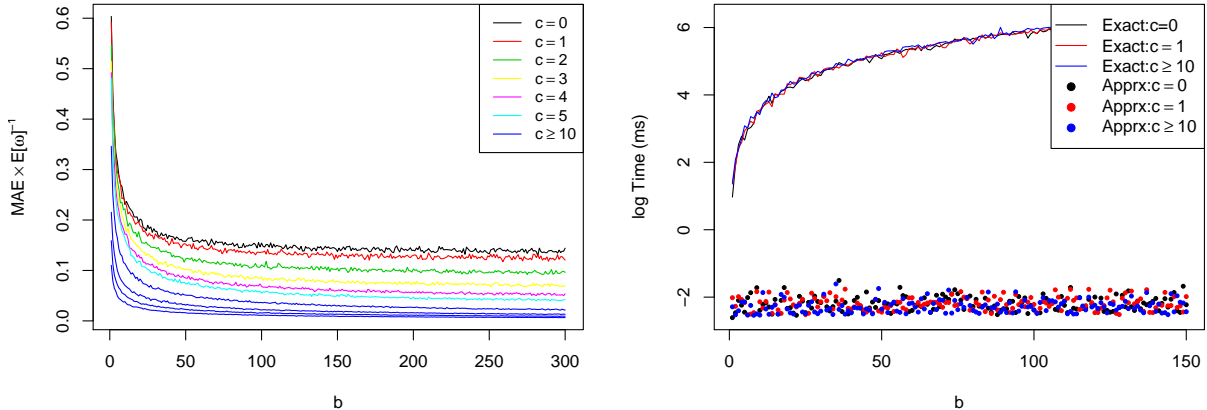


Figure 2: Simulation Errors and Times for the Pólya-Gamma Approximation

The update of the block assignments in the last step of the Gibbs sampler implies the computation of the posterior of the latent assignment probabilities for each node in the network (see step 10 in Appendix B.2). A naïve implementation will result in $\mathcal{O}(NKTB^2)$ time, which could be prohibitive for large N , specially if we update all z_i sequentially at each MCMC iteration. We recommend an annealed random-scan sampling that starts updating the entire network and exponentially decreases the number of vertices being updated to a small fraction as the estimation progress. This would allow the Gibbs sampler to initially explore a large space of possible clusterings at a higher computational cost, and then concentrate the estimation effort on the parameters defining the block dynamics while still allowing for some refinement in the assignments.

4. Simulation study

In this section we use synthetic data to compare the fitting capability and estimation time of the DMN model in Durante et al. (2017) with our DMBN model with block structure. We simulate multilayer networks with sizes ranging from $N = \{32, 64, 128, 256, 512\}$ and different levels of granularity: $B = \{5, 15, 45\}$. We also simulate networks from the DMN model without block structure. All networks have the same number of $K = 4$ layers and $T = 12$ time points, and are generated from a dynamic six-dimensional latent space, i.e. $R = H = 6$, with common smoothness $l_\mu = l_{\mu_p} = l_{\bar{x}} = l_x = 0.05$ over all components. Each latent coordinate are simulated from three predefined types of connectivity patterns: i) smoothed constant, ii) smoothed seasonal connectivity and iii) smoothed linear trend. Table 1 shows the parameter configuration that is used by both models during the simulations, which were performed on a cluster from the Swedish National Supercomputer Center (NSC-SNIC).

We estimated the models specified above to every simulated networks ten times with random initialization of block assignments and latent coordinates. Estimation times and performance metrics were averaged accordingly. Relative mean absolute errors (MAE) for estimating the true link probabilities are presented in Table 2. The results illustrate how the DMBN model takes advantage of the community structures to recover the link probabilities, effect that is more pronounced as the network

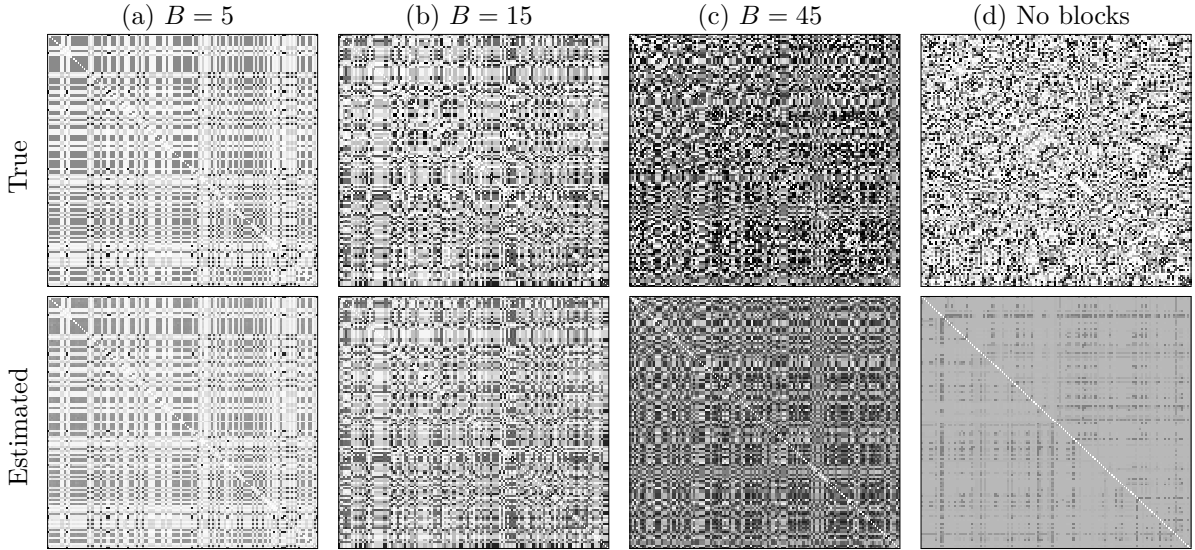


Figure 3: Illustrating the fitting capability of the DMBN with $B = 10$ blocks on data simulated from four multilayer networks with 5, 15, 45 and no blocks (DMN), as indicated in each column. All networks have $N = 128$ edges, $K = 4$ layers, and $T = 12$ time points. The top row displays the true link probabilities and the bottom row their estimated counterparts. The gray scale represent link probabilities going from $p(A_{ij}) = 0$ (white) to $p(A_{ij}) = 1$ (black).

size increases. For larger networks ($N = \{128, 256\}$) and clear block structure ($B = 5$) the DMBN model outperforms the DMN with relative MAE ratios of 3.65 and 4.20 respectively. On the other hand, the performance of the DMBN model decreases with granularity regardless of the network size. Absolute MAE's for both models are between 0.01 and 0.08. Note that for the DMN model the number of latent coordinates grows rapidly with N , and for networks of size $N = 512$ the estimation times exceeded the limit from the computing infrastructure, thus relative measures are not shown. The fact that the block-based model is not able to fully recover all individual link probabilities at full granularity is an expected outcome since this model tries to summarize the dynamic of groups of links using a very limited set of parameters. As the granularity increases towards the worst-case-scenario of a multilayer network where the dynamics of each link is generated by its own stochastic process and the block structure vanishes, the DMBN is expected to be less effective to fit the data and outperformed by the DMN.

Figure 3 shows the true and estimated probabilities from the DMBN on four dynamic multilayer networks with $N = 128$ nodes and different block structure. For each network ($B = 5, 15, 45$, and no block structure) the figure shows the probabilities from a randomly selected graph out of the entire set of $TK = 48$ graphs. The four images in the top row show the true probabilities, which appear clearly structured in (a-c) compared to the full-granularity graph in (d). In the bottom row we see how the DMBN is able to almost perfectly recover all probabilities when $B = 5$ and $B = 15$, is doing a decent job when $B = 45$ and, as expected, struggles to fit the DMN model without any block structure.

Table 3 presents the relative running times (originally in minutes) for all simulations. As expected, the capacity of the DMN model to capture network link dynamics at full granularity comes at the cost of time. The estimation of the DMN model is significantly slower compared to the DMBN, with running times ranging from twice ($N = 32$) to more than thirty times slower to those from the DMBN for the network with $N = 256$ nodes. For the DMBN the absolute estimation times are below one hour in most cases, and only grow noticeably when the network size is above $N = 256$, hence demonstrating the scalability of the model when $B \ll N$. This assumption may hold true for many real networks, such as social or transportation networks, where community structure naturally arises. In the next section we present a case study using real data, and evaluate the classification performance of the proposed

True B	Network Size				
	32	64	128	256	512
5	1.49	2.30	3.65	4.20	-
15	0.92	1.05	1.25	1.12	-
45	0.93	0.94	0.87	0.79	-
No blocks	1.13	1.11	0.92	0.73	-

Table 2: Relative Mean Absolute Error (MAE) ($\text{MAE}_{\text{DMN}}/\text{MAE}_{\text{DMBN}}$) for recovering the true probabilities from simulated data. The DMBN model is estimated with $B = 10$ blocks.

True B	Network Size				
	32	64	128	256	512
5	2.15	5.93	16.80	31.52	-
15	2.19	5.86	16.38	32.07	-
45	2.14	5.76	16.32	32.12	-
No blocks	2.11	5.57	16.24	31.16	-

Table 3: Relative computing time (minutes) of the DMN model compared to the DMBN model with $B = 10$ blocks.

model to predict markets within the US airport system, a classic example of a hub-and-spoke network.

5. Application to the US air transport network

Modeling complex transportation systems as dynamic multilayer graphs (Kivelä et al., 2014) has been recently attempted for e.g. air transportation (Cardillo et al., 2013), public transport (Gallotti and Barthelemy, 2015) or maritime networks (Ducruet, 2017). The majority of these contributions focus on the visual inspection of the graphs, or the temporal and multilayer analysis of the networks by means of static, layer-wise topological measures, with no use of statistical or machine learning models. In this case study we apply the model from Durante et al. (2017) and our community-based extension introduced in Section 3 to a real airline network with airports as nodes and airlines as layers. The dynamic and multilayer dimensions of the network are modeled jointly in a probabilistic fashion, and the stochastic block structure allows for interesting model-based clustering of airports. The data description is presented first, followed by two different study scenarios. In the first scenario we fit the DMN model to a small subnetwork of two airlines: Delta and Southwest. The objective is to investigate how the model estimates reflect changes in network structure due to the merger of Southwest and AirTran after 2011, and other events happened during the sample period. The second study features a full-scale forecasting application to a dynamic multilayer transport network with 80 airports and four airlines over a 10-year period. We compare both models in terms of classification performance and estimation times, and also investigate the resulting airport clusters from the DMBN. Table 5 summarizes the experimental setup and network data utilized in each case study. All experiments were implemented using R Open 3.4.2 (MKL support), and executed on an Intel i7 Dual-Core PC with 16 GB of RAM running Windows 10.

5.1. Data source and network description

We collected publically available airline ticket data from the Airline Origin and Destination Survey (BTS, 2019a), from which we create the air transportation graphs. Figure 4 shows the mainland US airports available from the survey along with their hub classification (FAA, 2019); we selected the $N = 80$ airports with the largest number of (departing) flights, over a period of ten years (2009-2018). These airports concentrate around 95% of the total network traffic. The survey provides quarterly data so the number of time steps will be $T = 40$. To create a multilayer network, we generate separate graphs corresponding to $K = 4$ major airlines: American Airlines, Delta, United/Continental and Southwest. Our choice of airlines is not random: after the mergers of Delta/Northwest (2009),

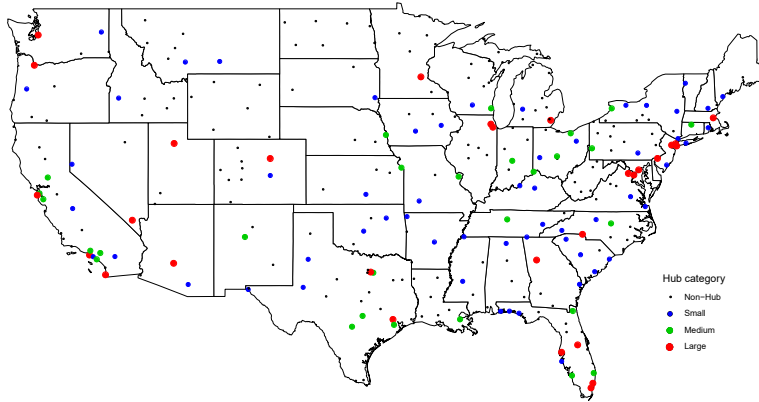


Figure 4: Mainland airports from the US air transport network, and their classification according to the Federal Aviation Administration (FAA, 2019).

United/Continental (2010), Southwest/AirTran (2011) and American Airlines/US Airways (2013), the resulting "big four" became the dominant airlines in the system. A graphical representation of the multilayer structure at the second quarter of 2011 is presented in Figure 5, and relevant network statistics in Table 4. We generated the multilayer graph using the library Pymnet (Kivelä, 2015). All indicators but the number of flights are based on the corresponding unweighted, undirected graphs. We see similar network characteristics among the full-service carriers, whereas Southwest stands out with a higher edge density and less centralized degree distribution, which agrees with the tendency of low-cost airlines to relax the hub-and-spoke model by developing a significant number of point-to-point markets (Doganis, 2019). Note also that there is only around 25% percent of edge-overlap between the different airlines, which justifies the use multilayer models.

Layer	Nodes	Edges	Density	ASPL	Degree	Flights
1 - AA	80	579	0.092	1.948	14.486	206,078
2 - DL	80	563	0.089	1.957	14.070	170,825
3 - UA	80	557	0.088	1.975	13.912	125,464
4 - WN	80	1,047	0.166	1.803	26.163	284,437
Combined	80	2,190	0.346	1.669	54.756	789,163

Table 4: Quarterly-averaged network statistics for the selected sample (2009-2018). AA: American Airlines, DL: Delta Airlines, UA: United Continental, WN: Southwest, ASPL: Average shortest path length.

5.2. Merger of Southwest and AirTran (2011)

When Southwest acquired AirTran in 2011, it was the first merger between low-cost carriers in US history. Prior to the merge, Southwest carried almost 90 million passengers in 2010, more than triple than AirTran, and operated point-to-point markets, in contrast to the hub-and-spoke structure of AirTran's network. The operation was appealing for Southwest, which not only had the opportunity to take over the network of its competitor, but also to enter Atlanta, which was at the time the only major US city without a strong presence of Southwest. This would help Southwest solidify its position as a dominant domestic low-cost carrier while adding some new international routes, mainly in the Caribbean, to its network. In this study, we investigate changes in the network graphs of Southwest and Delta, the dominant airline at Atlanta, as a consequence of the merger, and other potential causes between 2009-2018, using the dynamic multilayer model of Durante et al. (2017).

To that end, we fit the DMN model to a selected subset of the full multilayer graph shown in Figure 5, featuring $N = 40$ airports from Delta and Southwest ($K = 2$) networks, and keeping only the first

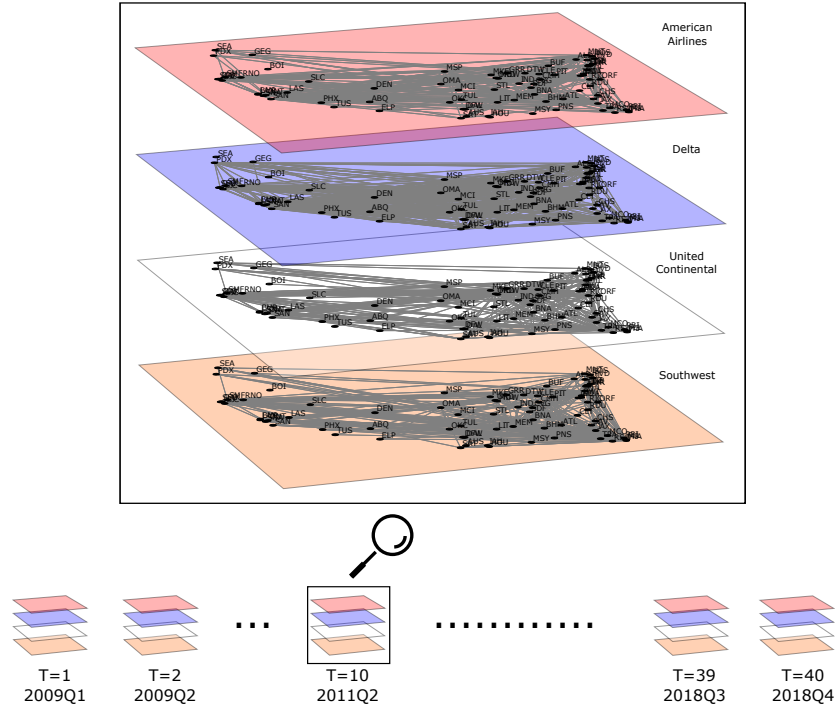


Figure 5: Dynamic multi-layered air transport network created from quarterly airline ticket data (2009-2018), and a snapshot at $T = 10$ (2011Q2).

quarter of every year ($T = 10$), see Table 5. Note that even though we will estimate $N(N-1)KT/2 = 15,600$ logits, this scenario is rather conservative compared to the half-million required for the full problem, hence the need for the community-based extension. We draw 5,000 posterior samples using similar hyperparameter values as for the simulations in Section 4, i.e. $R = H = 6$, with common smoothness $l_\mu = l_{\bar{x}} = l_x = 0.05$ over all components. Due to the bilinear forms in Eq. (1) the latent coordinates $\bar{x}(t)$ and $x^k(t)$ are not identified and their estimates should not be interpreted directly. We follow Hoff (2005) and calculate the posterior means of $\bar{x}(t)^T \bar{x}(t)$ for each t instead, which are identified, and then obtain estimators $\hat{\bar{x}}(t)$ by truncating the spectral decompositions at the R -th largest eigenvalue. The within-layer coordinates $x^k(t)$ are recovered using the same procedure, for every layer and time point. Since the estimated coordinates contain information about the connectivity profile of every airport i , it is straightforward to define cross and within layer vertex connectivity scores (VCS) as the euclidean norm of the coordinates, i.e.

$$\text{CL-VCS}_i(t) = \|\hat{\bar{x}}_i(t)\| \quad (9a)$$

$$\text{WL-VCS}_i^k(t) = \|\hat{x}_i^k(t)\| \quad (9b)$$

Figure 6 present both scores for all airports in the sample as a function of the number of connections (i.e. degree). There seems to be a strong linear correlation between the within-layer scores and the degree of an airport, which is not present in the cross-layer estimates. This is probably related to our choice of mixing a legacy (hub-and-spoke) and a low-cost (point-to-point) carrier in the experiment. If airlines are significantly different in their structure and routes, their connectivity patterns will be absorbed by the layer effects, and the interpretation of the cross-layer connectivity scores may not be possible by direct inspection. We compared the scores against more elaborated centrality indicators such as betweenness and closeness, with similar results. The fact that the latent coordinates, which

Description	Selected graphs by quarter and year										
Case study 1: model analysis		09	10	11	12	13	14	15	16	17	18
Only DMN model	Q1	×	×	×	×	×	×	×	×	×	×
Only Delta/Southwest (K=2)	Q2										
Subnetwork of N=40 airports	Q3										
	Q4										
Case study 2: forecasting		09	10	11	12	13	14	15	16	17	18
Both DMN/DMBN models	Q1	×	×	×	×	×	×	×	×	×	○
All airlines (K=4)	Q2	×	×	×	×	×	×	×	×	×	○
All airports (N=80)	Q3	×	×	×	×	×	×	×	×	×	○
	Q4	×	×	×	×	×	×	×	×	×	○

Table 5: General description of the case studies and the network data used. Fit/training graphs are marked with a cross (×), and test data with (○).

can be projected to future time steps, are related to topological properties from the underlying graph that determine the efficiency of air transportation in terms of e.g. passenger-kilometers (Kotegawa et al., 2014), is an interesting outcome from the model.

In Figure 7 (left) we look directly at the two largest components from the estimated cross-layer coordinates for all airports in 2009. Even though there is no apparent clustering structure, there exists a general pattern based on airline dominance at the airports, and the fact that we left American Airlines and Continental out of the experiment. Airports that are close to the origin are mostly American (e.g. Miami, Dallas Fort-Worth), US Airways (e.g. Philadelphia) or United/Continental (e.g. Houston, Chicago O’Hare) hubs, whereas the most outlying airports are hubs for Delta (e.g. Atlanta, Salt Lake City) or focus cities for Southwest (e.g. Midway), with the exception of Los Angeles and Boston. In this case, a visual inspection of the coordinates for a specific year and quarter is sufficient, but a proper cluster analysis would probably be the best choice for their interpretation over time. Back to the vertex scores, Figure 7 (right) presents the dynamic evolution of the cross-layer and within-layer VCS for Atlanta-Hartsfield. We see how the within-layer score for Southwest grows steadily after the merger with AirTran in 2011 and the subsequent expansion at Atlanta. As a consequence, the cross-layer score is pushed up as both airlines hold now an important presence in that vertex, while the score for Delta decreases slightly though remaining high. Similarly, once the cross-layer score is significantly increased, Southwest’s score starts to diminish as well, which could be an indication on how the model tries to leverage the different components of the logit during estimation.

Rank	CL-2009	CL-2018	DL-2009	DL-2018	SW-2009	SW-2018
1	SLC	↑ATL↑	ATL	ATL	MDW	MDW
2	LAX	LAX	SLC	SLC	DEN	↑DAL↑
3	DAL	LGA	JFK	MSP	LAS	DEN
4	OAK	↑MSP↑	LGA	DTW	PHX	STL
5	LGA	SLC	DTW	JFK	HOU	PHX
6	MSY	↑MCO↑	MSP	LAX	AUS	BNA
7	BWI	DAL	BOS	LGA	MCI	LAS
8	JFK	LAS	LAX	↑SEA↑	BWI	AUS
9	DTW	BWI	MCO	BOS	STL	HOU
10	LAS	OAK	TPA	↑LAS↑	BNA	BWI

Table 6: Top 10 airports according to estimated vertex connectivity scores 2009-2018. CL: cross-layer VCS, DL: within-layer VCS for Delta, SW: within-layer VCS for Southwest. Up-arrows ↑X↑ indicate that airport X climbed the ranks up to the top-10 between 2009-2018.

Table 6 presents airport rankings according to estimated vertex connectivity indices for the sample period. Overall, we get the expected actors at the top of the ranks, particularly at the airline (layer)

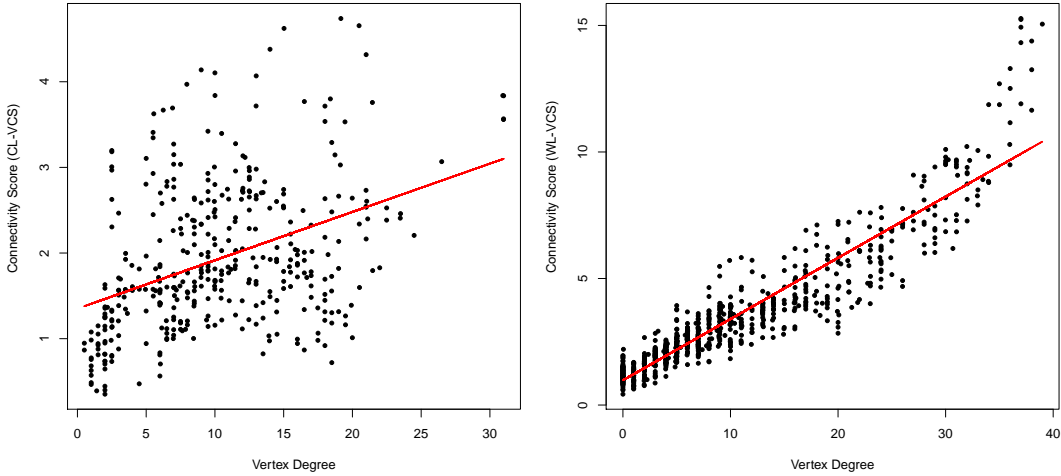


Figure 6: Estimated Vertex Connectivity Scores (VCS) for all airports, time points and layers, against the original airport degrees. Left: cross-layer scores. Right: within-layer scores (both Southwest and Delta).

level: Atlanta, Salt Lake City and Minneapolis lead Delta’s network, whereas Chicago Midway, Denver, Las Vegas and Dallas-Love are the top performers for Southwest. In the cross-layer rankings, we notice the rising of Minneapolis and Atlanta between 2009-2018, which is probably due to their acquisition by Delta and Southwest after the mergers with Northwest (2008) and AirTran (2011), respectively. In 2014, Delta increased its presence at Seattle airport in order to open a transoceanic hub, therefore entering into direct competition in the domestic market with Alaska Airlines at their major base. This is reflected on Delta’s within layer rankings with Seattle climbing from the 19-th to the 8-th position. From the Southwest’s perspective, Dallas Love-Field appears as the airport with largest increase in within-layer connectivity. This is an expected result: after the repealing of 1979’s Wright Amendment, which prohibited flights from Dallas Love-Field outside Texas and its neighboring states in order to protect Dallas Fort-Worth, Southwest greatly expanded at the former with 15 new routes in late 2014 (CAPA, 2015). In Figure 8 (top row) we illustrate the model’s ability to capture the network’s dynamics during this expansion of Southwest at Love-Field, focusing on the new routes to/from Washington-Reagan, Portland and Tampa. Note how the underlying Gaussian processes that drive the logits adjust rapidly to changes in the network in all cases. Here the model’s flexibility in latent space has clearly paid off, despite the lack of exogenous (e.g. passenger traffic) information outside the adjacency matrices. We have experimentally verified that the estimated link probabilities are not sensitive to reasonable changes in the degree of shrinkage of the latent coordinates (as controlled by the hyperparameters a_1, a_2 in the Gamma prior), which control the effective dimensionality of the latent space. Similarly, the estimates are also robust to variation in the size of the latent coordinates R, H , and the prior smoothness of the corresponding Gaussian processes. It is important to remark that the flexibility in latent space is due not only to the magnitude (e.g. connectivity scores) but also to the alignment (i.e. angles) of the vectors. For instance, the estimated cross-layer components can be written as $\hat{x}_i(t)^T \hat{x}_j(t) = \cos \theta_{ij}(t) \times \text{CL-VCS}_i(t) \times \text{CL-VCS}_j(t)$, where the angles $\theta_{ij}(t)$ between the latent airport coordinates are a function of time. We finally corroborate this for our example in Figure 8 (bottom row): the cross-layer and layer-wise (Southwest) latent components of the new markets (2009-2018) are closer in angle to those of Dallas Love-Field.

5.3. Dynamic multilayer forecasting of the US air transport network

Despite its effectiveness, as we have just confirmed, fitting the original DMN model to very large graphs is not practical due to the over-parametrization and subsequent high estimation times. Here we test our proposed model extension by fitting and forecasting a large dynamic multilayer graph

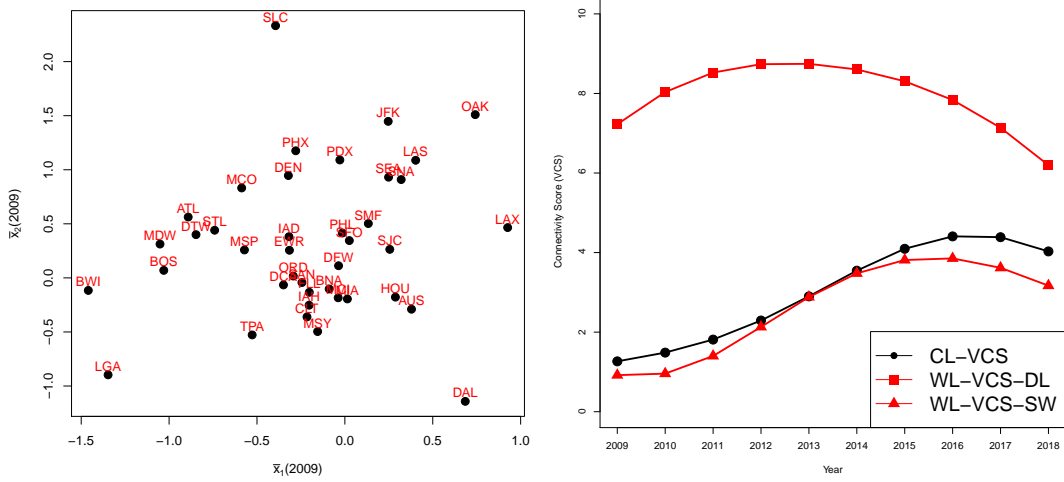


Figure 7: Left: estimated cross-layer coordinates (two largest components) for all airports in 2009. Right: Vertex Connectivity Scores (VCS) for Atlanta-Hartsfield. See Appendix D for the IATA airport codes.

using all available airline data. The complete network features $N = 80$ airports, $K = 4$ airlines and $T = 40$ time steps corresponding to quarters between 2009-2018. We compare both models in terms of classification accuracy and estimation times, and also investigate whether the block-wise structure of the DMBN model is able to reveal meaningful airport communities.

First we compare the performance of the DMN with the DMBN model. For both models we choose a $R = H = 2$, and a very smooth progression over time $l_\mu = l_{\mu_p} = l_{\bar{x}} = l_x = 5 \times 10^{-5}$. We use the first nine years of the sample (36 quarters) for training the model, i.e. $t = \{t_1, \dots, t_{36}\}$, and the last year for out-of-sample testing. Both models were run for 5,000 MCMC iterations and 20% burn-in, with a random-scan for the DMBN. Computing the posterior predictive distribution for the edge probabilities in the test sample $t^* = \{t_{37}, \dots, t_{40}\}$ is straightforward within the current Gibbs sampling framework, see Step 11 in Appendix B.2. Figure 9 (top-left) shows the ROC curves over the test data for the DMBN with $B = \{3, 6, 9\}$ blocks and the DMN. The DMN turns out to be a very accurate classifier, but is computationally very costly as it estimates $N(N-1)/2KT = 505,600$ logits, in contrast to the $B(B+1)/2KT = 14,400$ from the DMBN with $B = 9$ blocks. The performance of the DMBN model increases with B and takes substantially less time to estimate; estimation times (Figure 9, top-right) for the DMBN range from 25 minutes ($B = 3$) to 1.5 hours ($B = 9$), and are at least one order of magnitude faster than the DMN, which needs almost 19 hours to be estimated. The layer-wise ROC curves presented below for the DMBN with $B = 9$ blocks (left), and the DMN (right) also show how the least structured airline network (Southwest) is the most difficult to predict.

Figure 10 presents some adjacency matrices from the multilayer network, and their estimated edge probabilities calculated from the posterior samples of the DMBN model with $B = 9$ blocks. All matrices are 80×80 in size, and their rows are ordered according to the airport's IATA codes (see Appendix D). Most adjacency matrices (top row) present a clear hub-and-spoke layout, with few dominant airports connected to all other nodes at a given layer, which is captured well by the model through the estimated probabilities (bottom row). Note that probability matrices in Figure 10 (bottom row) are not ordered according to blocks but to airport codes, thus the block structure resulting from the DMBN model is not clearly visible. The first column shows the network of American Airlines at the last quarter of 2009, from which we see how the model learned the connectivity patterns from the adjacency matrix, assigning the highest probabilities to edges connected to Charlotte, Dallas Fort-Worth, Miami, Chicago O'Hare and Philadelphia. Having the latent block coordinates $\bar{x}_{z_i}(t)$ entering as a bilinear form (Hoff, 2005) is convenient here to capture the cross-like patterns exhibited by these hubs, as airports with larger magnitudes in their latent space will increase their connectivity with respect to

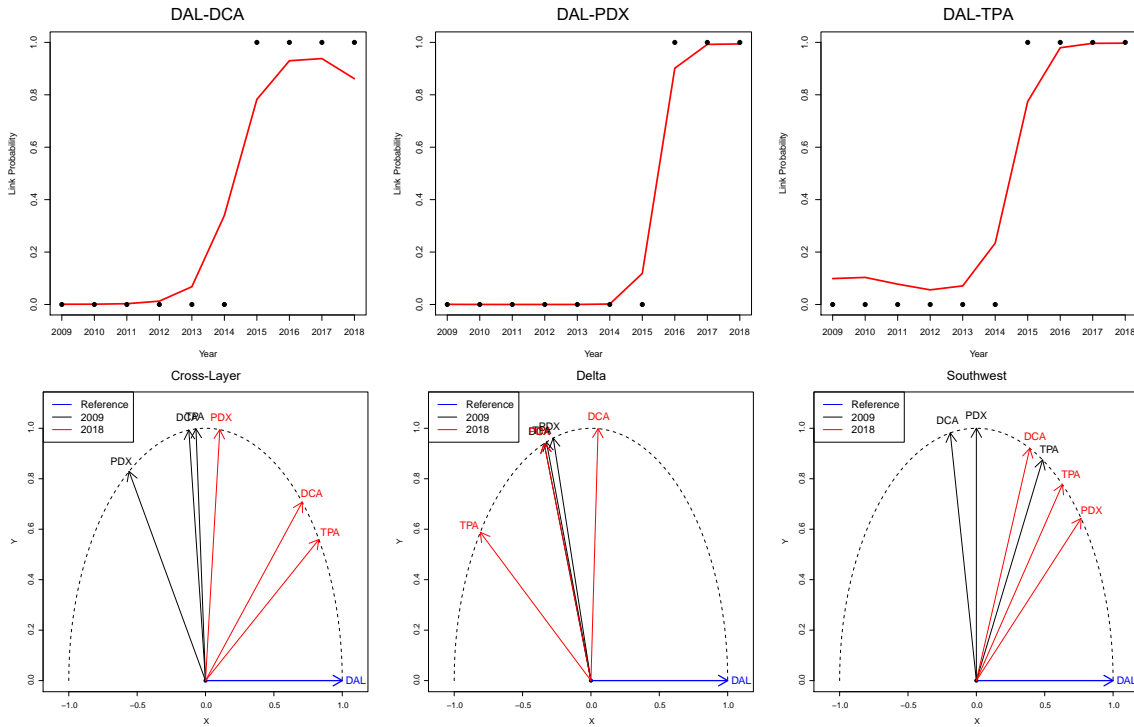


Figure 8: Top row: Estimated link probabilities for three new Southwest routes from Dallas Love-Field (DAL): Washington-Reagan (DCA - left), Portland (PDX - center) and Tampa (TPA - right). Black dots are the original data in the corresponding adjacency matrices. Bottom row: Angles between the estimated latent vectors of DAL, and the rest of airports, 2009-2018. We use normalized vectors within the unit circle to represent angle differences between cross-layer (left) and within-layer (Delta and Southwest, center and right, respectively) coordinates.

every other node in the network, regardless of the block they belong to. The estimated edge probabilities for Delta in the third quarter of 2009 (second column) seem to have captured the most relevant patterns, corresponding to the connections of Delta’s major hubs, i.e. Atlanta, Detroit, Los Angeles, La Guardia, Minneapolis and Salt Lake City. Similar results are obtained for United/Continental in 2015 (third column) with Newark, Dulles, Houston International and San Francisco, although some more noise is appreciated in the estimated probabilities. The last column of Figure 10 shows the one-quarter-ahead predicted edge probabilities in the test set for American Airlines.

Airline densities and airport degrees can be readily calculated from the posterior edge probabilities (Eq. 10a,10b), both for in-sample and out-of-sample predictions. Figure 11 presents observed and estimated network densities for all airlines during the sample period, which range from 0.05 to 0.2. In all cases the estimated densities fit almost perfectly the observed data, and forecasts lie within the 95% posterior intervals. Note that the density forecasts are not a mere projection from a univariate time-series, as Figure 11 may suggest: here the entire multilayer graph has been projected forward in time using the smoothness from the Gaussian processes. Future densities and degree distributions are then calculated from the predicted multilayer networks. American Airlines appears as the airline with the most stable network density, in a similar manner as Delta after it absorbed Northwest in 2010. United/Continental shows a marked seasonal effect after the merge of their former airlines in 2012, perhaps due to network restructuring. Southwest is the only airline that grows steadily in density

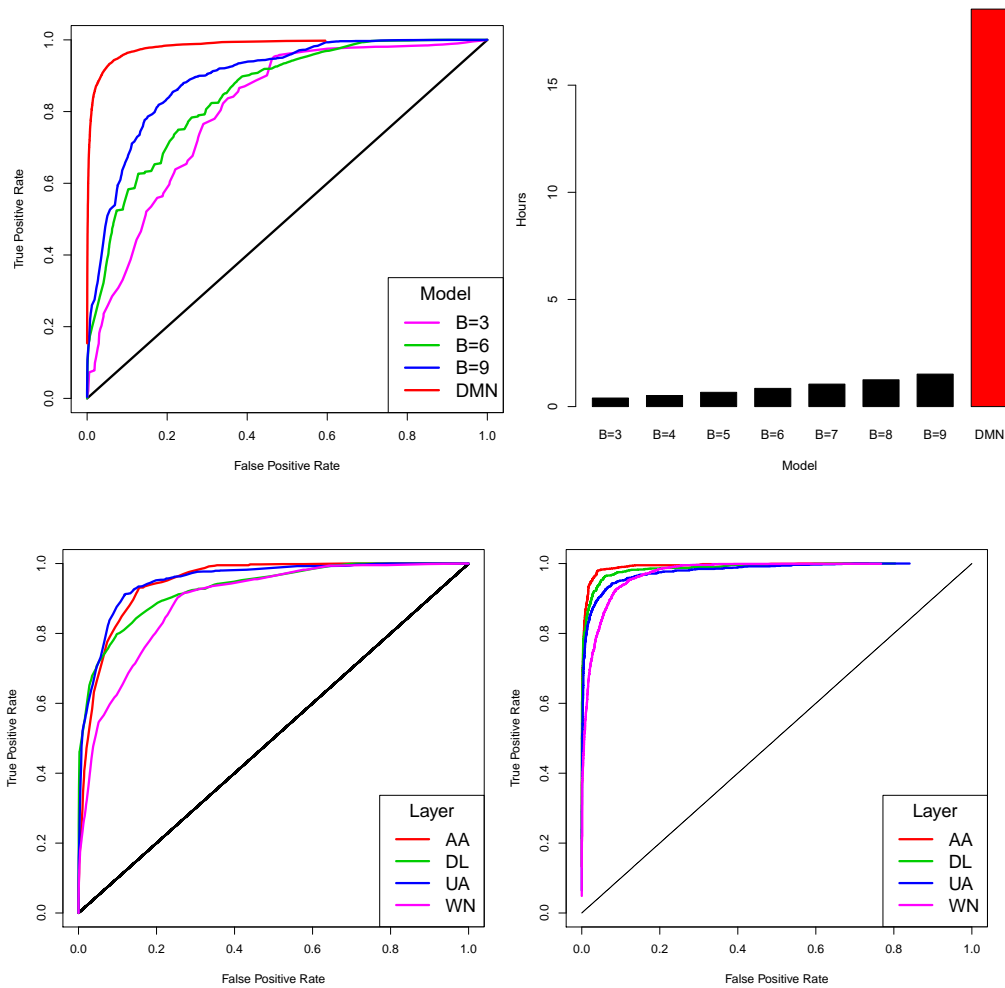


Figure 9: Top: ROC curves (left) and estimation times (right) for the proposed model with increasing number of blocks and the DMN (Durante et al., 2017). Bottom: layer-wise ROC curves from the proposed model with $B = 9$ (left) and the DMN (right).

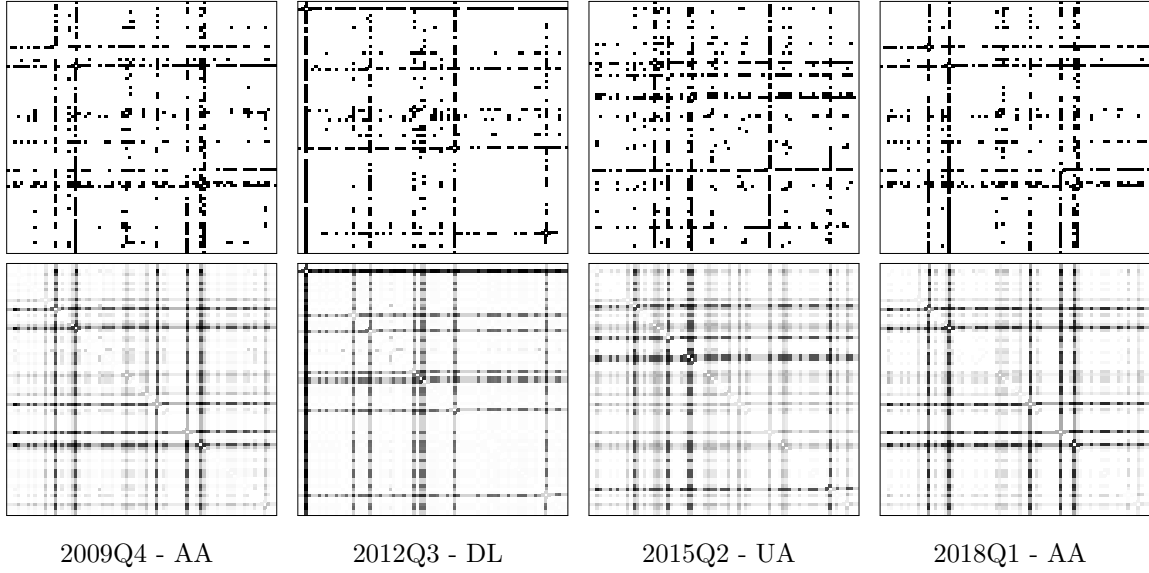


Figure 10: Observed adjacency matrices (top row) and estimated edge probabilities (bottom row) on selected graphs from the multilayer airline network. The first three columns present estimates from graphs within the training set, whereas the last column shows the one-quarter-ahead estimated probabilities.

during the sample period, with noticeable seasonality after 2013.

$$D^k(t) = \mathbb{E} \left[\sum_{i=2}^N \sum_{j=1}^{i-1} A_{ij}^k(t) / (N(N-1)/2) \right] = \sum_{i=2}^N \sum_{j=1}^{i-1} \pi_{z_i z_j}^k(t) / (N(N-1)/2) \quad (10a)$$

$$d_i^k(t) = \mathbb{E} \left[\sum_{j \neq i} A_{ij}^k(t) \right] = \sum_{j \neq i} \pi_{z_i z_j}^k(t) \quad (10b)$$

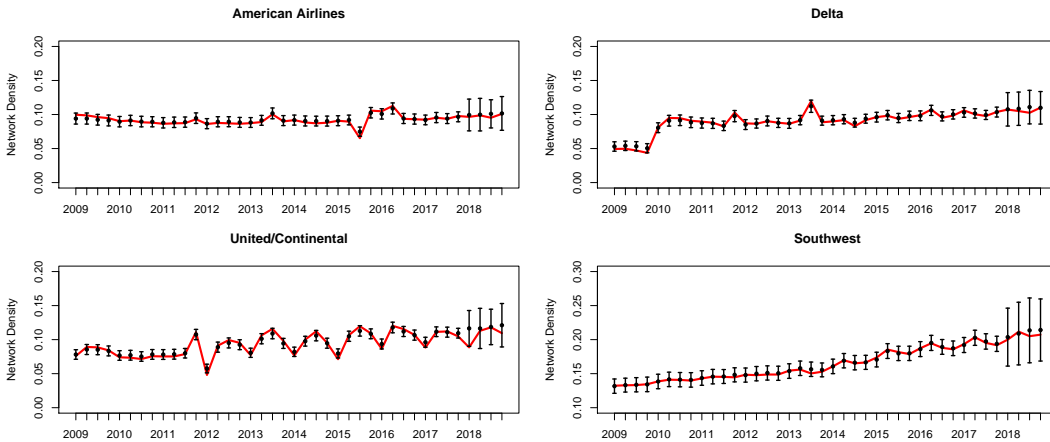


Figure 11: Estimated (black) and observed (red) network densities.

Table 7 lists the nine airport clusters found by the DMBN model. The clustering structure becomes apparent after computing the matrix of posterior probabilities that two nodes are in the same block, which is invariant with respect to the block labels. Clusters have been formed both layer-wise and also

according to the connectivity dynamics of each airport. The first cluster is the largest, and contains 33 airports that are mainly small and mid-sized Southwest airports, with the exception of Honolulu, Cleveland and Memphis. Cluster 2 aggregates airports with a rising number of Southwest connections, the outliers here would be Boston, NY La Guardia, Seattle and Washington Reagan. The third, fourth and sixth clusters represent the bulk of the major hubs from American Airlines, Delta, and Southwest respectively, whereas Chicago Midway stands alone in cluster 5 as the largest focus city for Southwest, with a 96% of market share (BTS, 2019b). The three airports in cluster 7 are fast-growing Southwest bases, with Dallas Love Field and Houston Hobby among the fastest growing airports in the US in the last decade. Cluster 8 groups a number of large hubs with little presence of Delta, with the exception of Los Angeles, and cluster 9 features large United/Continental hubs. Figures 12 and 13 present the observed and estimated degrees (Eq. 10b) for two clusters to assess the effect of the stochastic blockmodeling on learning the dynamics of the multilayered network. Note how the estimated Gaussian process for the edge probabilities in each block captures the average dynamics from all airports belonging to that block.

Cluster	Airports
$\hat{p} = 1$	ABQ, ALB, BDL, BHM, BOI, BUF, BUR, CHS, CMH, CVG, ELP, GEG, GRR, HNL, ISP, JAX, LIT, MEM, MHT, OGG, OKC, OMA, ONT, ORF, PBI, PNS, PVD, RIC, RNO, SAV, SDF, TUL, TUS
$\hat{p} = 2$	AUS, BOS, CLE, DCA, IND, LGA, MCI, MKE, MSY, PDX, PIT, RDU, RSW, SAN, SAT, SEA, SJC, SMF, SNA
$\hat{p} = 3$	CLT, DFW, JFK, MIA
$\hat{p} = 4$	ATL, DTW, MSP, SLC
$\hat{p} = 5$	MDW
$\hat{p} = 6$	BNA, BWI, FLL, LAS, MCO, STL, TPA
$\hat{p} = 7$	DAL, HOU, OAK
$\hat{p} = 8$	DEN, LAX, PHL, PHX
$\hat{p} = 9$	EWR, IAD, IAH, ORD, SFO

Table 7: Estimated airport clusters. IATA airport codes in Appendix D.

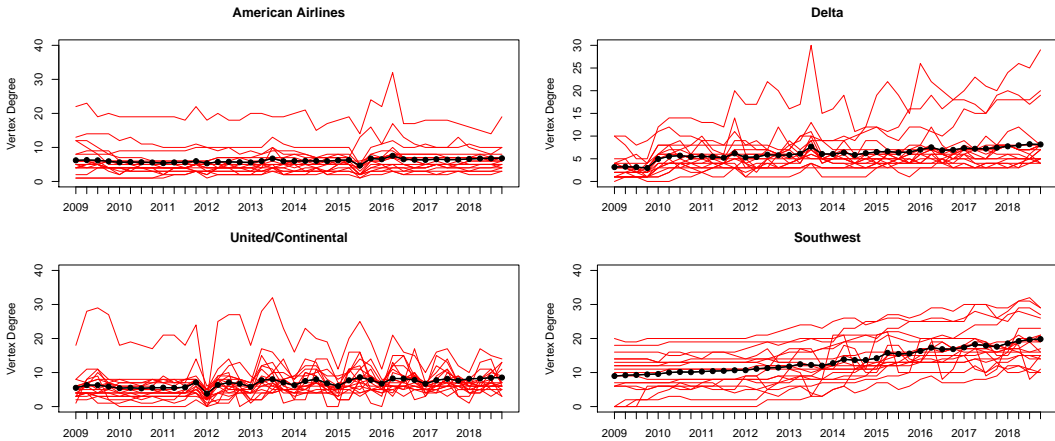


Figure 12: Observed (red) and estimated (black) vertex degrees for block 2.

We finally benchmark the DMN and DMBN forecasting performance against several popular, non-probabilistic, algorithms. Link prediction is a common task in network science, where a large proportion of methods are based on similarity metrics (Lü and Zhou, 2011; Martínez et al., 2016). Similarity-based algorithms define a function, usually based on the topology of the graph, to assign a similarity score

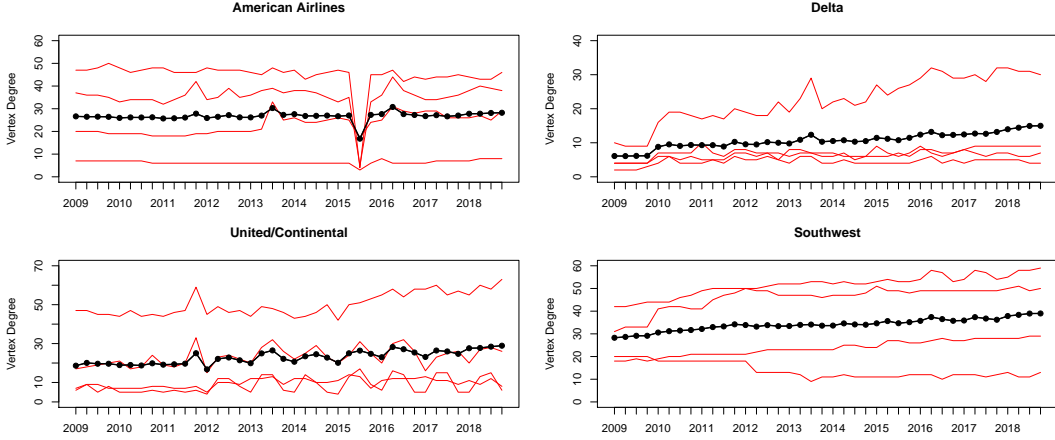


Figure 13: Observed (red) and estimated (black) vertex degrees for block 8.

between every pair of nodes in the network. These scores can be used as input for a binary classifier that predicts the existence or non-existence of links between nodes. We choose five similarity-based algorithms: i) Common Neighbors (CN)-(Newman, 2001), ii) Adamic-Adar Index (AA)-(Adamic and Adar, 2003), iii) Katz Index (Katz)-(Katz, 1953), iv) Random walk with restart (RWR), based on PageRank algorithm (Brin and Page, 1998), and v) Local Path Index (LPI)-(Zhou et al., 2009). The first two indexes use the local topology to calculate scores whereas Katz and RWR are global methods that use all available information in the graph; LPI is based on a mixed strategy. These algorithms can be readily implemented in e.g. R for link prediction (Kolaczyk and Csárdi, 2014; Bojanowski and Chrol, 2018). The selected methods are originally defined for single-layered non-dynamic graphs. We will therefore apply the algorithms layerwise, but extending them to a dynamic setting, as follows. Let $\text{score}_{ij}^k(t)$ be the similarity score between nodes i, j at layer k and time t . A straightforward way to account for time dynamics is to use a simple exponential smoother,

$$S_{ij}^k(t) = \alpha \text{score}_{ij}^k(t) + (1 - \alpha) S_{ij}^k(t - 1), \quad t > 1, \quad (11)$$

$$S_{ij}^k(1) = \text{score}_{ij}^k(1) \quad (12)$$

where $\alpha \in [0, 1]$ is the smoothing parameter. The recursion above can be applied on each layer until we obtain $S^k(t = t_{36})$, a matrix of scores that summarizes the information contained in the training data on that layer, and that can be used to classify/predict the links on the test graphs $A^k(t = t_{37}, \dots, t_{40})$. In Figure 14 we present the ROC curves and the area under the curve (AUC) for the DMN and DMBN with 9 blocks (DMBN9), and for the similarity-based prediction algorithms with $\alpha = 1$, i.e. a random-walk. We see that the classifiers based on the global indicators (Katz and RWR) are almost as good as the DMN. Local and quasi-local models (CN, AA, and LPI) are faster alternatives comparatively, but with a reduced predictive performance. Table 8 presents evaluation metrics for all algorithms at two different levels of α . The classification threshold for each model has been chosen to maximize the F1 measure. Overall, the DMN and the Katz index are the best probabilistic and similarity-based classifiers, respectively. Probabilistic models yield better results in term of precision/recall and the combined F1 measure. The classification performance of similarity-based algorithms improves as their scores take more information from the recent graphs in the series due to the smoothing. Still, while some of the similarity-based methods are competitive as pure link-prediction devices, their outcome (i.e. the score matrices) can be difficult to interpret, and the insights from such models are quite limited. As we have shown in the two case studies, probabilistic multilayer dynamic models have the important advantage of offering, among other possibilities, probabilistic forecasts, temporal network analysis from inferred latent coordinates, and community detection.

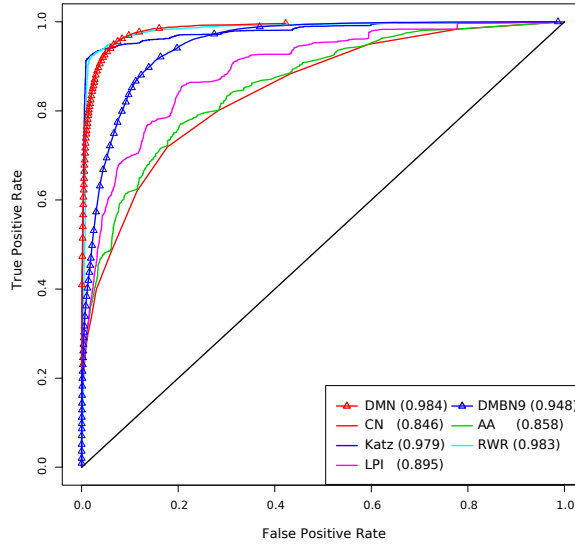


Figure 14: ROC curves for probabilistic and similarity-based link prediction methods. The numbers in parenthesis are the areas under the curve (AUC).

5.4. Some practical implications in air transportation

The network predictions provided by the DMN and DMBN models can have a variety of applications. From a regulatory perspective, we can mention merger screening. In a post-covid setting with further concentration predicted for the airline sector (Budd et al., 2020), major consolidations in the US had often involved thousands of city-pair markets that must be screened in order to identify those where the merger would lead to an excessive increase in monopolistic power. These models can predict the system-wide evolution of market shares and route concentration post-merger to pinpoint the main routes of concern for competition authorities, who might then formulate a series of remedial divestitures to mitigate the anticompetitive threats or reject the merger altogether. From a network planning perspective, our model can aid in the identification of new or potentially underserved routes, a process that would require the addition of demand and supply factors into the prediction. These would include, among others, price levels, catchment areas, substitute travel modes, and even the evolving nature of aircraft technology as it affects fuel efficiency and break-even load factors.

We have obtained promising results both in terms of model expressiveness and prediction power by focusing on three full-service-carriers plus Southwest within the US market, but these may not generalize to a different case study. The application to different markets would require to carefully set up the model and experiments for that particular case. A bigger coverage of secondary cities, with the corresponding sacrifice of computational time, would be needed to properly characterize the networks of low-cost carriers in the US, with the added challenge, in terms of accuracy, of training the model to account for the operation of narrow-body aircraft by LCCs like Spirit or Frontier on relatively thinner coast-to-coast routes (Soyk et al., 2018). An additional level of complexity would be present if applying the model to the less concentrated European airline market, where most big carriers operate single or dual-hub strategies and there is more integration with high-speed rail, bringing both competition and collaboration opportunities to air carriers and thus playing a key role in shaping the multilayer network dynamics.

Model ($\alpha = 1$)	Precision	Recall	F_1	AUC
DMN	(0.933)	0.950	0.941	0.984
DMBN - 9 Blocks	0.855	(0.914)	0.884	0.948
Common Neighbors	0.441	0.620	0.515	0.846
Adamic-Adar	0.526	0.590	0.557	0.858
Katz Index	0.936	0.913	(0.924)	0.979
Random Walk Restart	0.908	0.905	0.907	(0.983)
Local Path Index	0.566	0.678	0.617	0.895
Model ($\alpha = 0.4$)	Precision	Recall	F_1	AUC
DMN	(0.933)	0.950	0.941	0.984
DMBN - 9 Blocks	0.855	0.914	0.884	0.948
Common Neighbors	0.511	0.577	0.542	0.855
Adamic-Adar	0.519	0.606	0.559	0.863
Katz Index	0.945	0.915	(0.930)	0.992
Random Walk Restart	0.895	(0.922)	0.908	(0.988)
Local Path Index	0.564	0.673	0.613	0.897

Table 8: Classification metrics for probabilistic and similarity-based link prediction methods, with α as temporal smoothing parameter. Best model is indicated in bold font, and runner-up in parenthesis.

6. Conclusion

We present dynamic multilayer network methods with potential applications to transportation networks due to their potential to model and forecast time series of complex graphs. Flexible time series analysis is obtained by modeling the probability of edges between vertices through latent Gaussian processes. The block-based extension is natural for many real networks, such as transportation networks, where community structure naturally arises, and makes it possible to substantially improve the scaling of Bayesian inference algorithms to larger networks. Specifically, the models have the potential to enhance the analysis of transportation networks due to their ability to: i) capture the dynamic, multi-layered nature of most transport networks, ii) model both endogenous and exogenous effects underlying such dynamics, iii) perform out-of-sample network forecasting, and iv) scale to reasonably large problems. The models and Bayesian inference methodology are illustrated on a sample of 10-year quarterly data from four major US airlines: American, Delta, United/Continental and Southwest.

We take advantage from the fact that important network restructuring and merges within the US air transportation system takes place during the sample period (2009-2018), and assess the ability of the models in reflect those changes. Results show how the estimated latent parameters from the models are related to the airline’s connectivity dynamics, reflecting e.g. the entrance of Southwest into Atlanta after its merge with AirTran (2011), or its expansion at Dallas Love-Field in 2014. We show also how the extended model is able to capture the hub-and-spoke nature of the air transport network, and to project the entire multilayer graph into the future for out-of-sample full network forecasts, which differs from the current practice of visual analysis of static topological indicators. The stochastic blockmodeling allows for a time-series clustering of the airports’ connectivity dynamics, and the identification of relevant communities, while keeping estimation times within reasonable limits.

Several interesting extensions of the model are possible. For example, explicit modeling of three-way dependencies, which are common in e.g. air transportation. Extending the model to accommodate exogenous network covariates or layer-wise stochastic blocks is straightforward. Better methods for handling label-switching (Celeux et al., 2019) in multi-layered networks would make it easier to interpret some aspects of the extended model’s results. For very large network problems, variational approximations within the Pólya-Gamma framework (Zhou et al., 2012) may be a good strategy to reduce estimation times.

Acknowledgments

This work was partially supported by the Wallenberg AI, Autonomous Systems and Software Program (WASP) funded by the Knut and Alice Wallenberg Foundation.

References

- Adamic, L. A. and Adar, E. (2003). Friends and neighbors on the web. *Social networks*, 25(3):211-230.
- Aicher, C., Jacobs, A. Z., and Clauset, A. (2014). Learning latent block structure in weighted networks. *Journal of Complex Networks*, 3(2):221-248.
- Airoldi, E. M., Blei, D. M., Fienberg, S. E., and Xing, E. P. (2008). Mixed membership stochastic blockmodels. *Journal of Machine Learning Research*, 9(Sep):1981-2014.
- Alkaabneh, F., Diabat, A. and Elhedhli, S. (2019). A Lagrangian heuristic and GRASP for the hub-and-spoke network system with economies-of-scale and congestion. *Transportation Research Part C: Emerging Technologies*, 102:249-273.
- Barabási, A.-L. (2016). *Network Science*. Cambridge university press.
- Barabási, A.-L. and Albert, R. (1999). Emergence of scaling in random networks. *Science*, 286(5439):509-512.
- Bhattacharya, A. and Dunson, D. B. (2011). Sparse bayesian infinite factor models. *Biometrika*, pages 291-306.
- Bojanowski, M. and Chrol, B. (2018). *linkprediction: Link Prediction Methods*, R package version 1.0-0. <https://CRAN.R-project.org/package=linkprediction>.
- Brin, S. and Page, L. (1998). The anatomy of a large-scale hypertextual web search engine. *Computer networks and ISDN systems*, 30(1-7):107-117.
- BTS (2019a). *Airline Origin and Destination Survey (DB1B)*. Bureau of Transportation Statistics, US Department of Transportation.
- BTS (2019b). *Airport Statistics*. Bureau of Transportation Statistics, US Department of Transportation.
- Budd, L., Ison, S. and Adrienne, N. (2020). European airline response to the COVID-19 pandemic—Contraction, consolidation and future considerations for airline business and management. *Research in Transportation Business & Management*, 37:100578.
- Cadarso, L. and de Celis, R. (2017). Integrated airline planning: Robust update of scheduling and fleet balancing under demand uncertainty. *Transportation Research Part C: Emerging Technologies*, 81:227-245.
- Cardillo, A., Gómez-Gardenes, J., Zanin, M., Romance, M., Papo, D., Del Pozo, F., and Boccaletti, S. (2013). Emergence of network features from multiplexity. *Scientific reports*, 3:1344.
- CAPA (2015). *American Airlines and Southwest Airlines in Dallas DFW and Love: competition revives as Wright ends*. CAPA - Centre for Aviation (online). <http://centreforaviation.com>.
- Celeux, G., Kamary, K., Malsiner-Walli, G., Marin, J.-M., and Robert, C. P. (2019). Computational solutions for Bayesian inference in mixture models. In Fruhwirth-Schnatter, S., Celeux, G., and Robert, C., editors, *Handbook of Mixture Analysis*, chapter 5, pages 73-96. CRC Press.
- Crane, H. (2018). *Probabilistic foundations of statistical network analysis*. CRC Press.
- Daudin, J.-J., Picard, F., and Robin, S. (2008). A mixture model for random graphs. *Statistics and computing*, 18(2):173-183.
- de Wit, J. G. and Zuidberg, J. (2016). Route churn: an analysis of low-cost carrier route continuity in europe. *Journal of Transport Geography*, 50:57-67.
- Devroye, L. (2009). On exact simulation algorithms for some distributions related to jacobi theta functions. *Statistics & Probability Letters*, 79(21):2251-2259.
- Doganis, R. (2019). *Flying Off Course: Airline Economics and Marketing*. Routledge.
- Ducruet, C. (2017). Multilayer dynamics of complex spatial networks: The case of global maritime flows (1977-2008). *Journal of Transport Geography*, 60:47-58.

- Ducruet, C. and Notteboom, T. (2012). The worldwide maritime network of container shipping: spatial structure and regional dynamics. *Global networks*, 12(3):395–423.
- Durante, D. and Dunson, D. B. (2014). Nonparametric bayes dynamic modelling of relational data. *Biometrika*, 101(4):883–898.
- Durante, D., Mukherjee, N., and Steorts, R. C. (2017). Bayesian learning of dynamic multilayer networks. *Journal of Machine Learning Research*, 18(43):1–29.
- Erdős, P. and Renyi, A. (1959). On random graphs. i. *Publicationes Mathematicae (Debrecze)*, 6:290–297.
- FAA (2019). *National Plan of Integrated Airport Systems (NPIAS) 2019-2023*. Federal Aviation Administration, US Department of Transportation.
- Fortunato, S. (2010). Community detection in graphs. *Physics reports*, 486(3-5):75–174.
- Gallotti, R. and Barthelemy, M. (2015). The multilayer temporal network of public transport in great britain. *Scientific data*, 2:140056.
- Guimera, R., Mossa, S., Turtschi, A., and Amaral, L. N. (2005). The worldwide air transportation network: Anomalous centrality, community structure, and cities’ global roles. *Proceedings of the National Academy of Sciences*, 102(22):7794–7799.
- Han, Q., Xu, K., and Airoldi, E. (2015). Consistent estimation of dynamic and multi-layer block models. In *International Conference on Machine Learning*, pages 1511–1520.
- Hoff, P. D. (2005). Bilinear mixed-effects models for dyadic data. *Journal of the American Statistical association*, 100(469):286–295.
- Hoff, P. D., Raftery, A. E., and Handcock, M. S. (2002). Latent space approaches to social network analysis. *Journal of the American Statistical association*, 97(460):1090–1098.
- Holland, P. W., Laskey, K. B., and Leinhardt, S. (1983). Stochastic blockmodels: First steps. *Social networks*, 5(2):109–137.
- Holland, P. W. and Leinhardt, S. (1981). An exponential family of probability distributions for directed graphs. *Journal of the American Statistical association*, 76(373):33–50.
- Ishiguro, K., Iwata, T., Ueda, N., and Tenenbaum, J. B. (2010). Dynamic infinite relational model for time-varying relational data analysis. In *Advances in Neural Information Processing Systems*, pages 919–927.
- Jasny, B. R., Zahn, L. M., Marshall, E., and Cho, A. (2009). Complex systems and networks, special issue. *Science*, 406:405–432.
- Katz, L. (1953). A new status index derived from sociometric analysis. *Psychometrika*, 18(1):39–43.
- Kivelä, M. (2015). *Pymnet: Multilayer Networks Library for Python*. <http://www.mkivela.com/pymnet>.
- Kivelä, M., Arenas, A., Barthelemy, M., Gleeson, J. P., Moreno, Y., and Porter, M. A. (2014). Multi-layer networks. *Journal of complex networks*, 2(3):203–271.
- Kolaczyk, E. D. (2009). *Statistical Analysis of Network Data: Methods and Models*. Springer Publishing Company, Incorporated, 1st edition.
- Kolaczyk, E. D. and Csárdi, G. (2014). *Statistical analysis of network data with R*. Springer.
- Kolaczyk, E. D. (2017). *Topics at the Frontier of Statistics and Network Analysis:(re) visiting the Foundations*. Cambridge University Press.
- Kotegawa, T., DeLaurentis, D. and Sengstacken, A. (2010). Development of network restructuring models for improved air traffic forecasts. *Transportation Research Part C: Emerging Technologies*, 18(6):937–949.
- Kotegawa, T., Fry, D., DeLaurentis, D. and Puchaty, E. (2014). Impact of service network topology on air transportation efficiency. *Transportation Research Part C: Emerging Technologies*, 40:231–250.
- Lü, L. and Zhou, T. (2011). Link prediction in complex networks: A survey. *Physica A: statistical mechanics and its applications*, 390(6):1150–1170.
- Martínez, V., Berzal, F. and Cubero, J.C. (2016). A survey of link prediction in complex networks. *ACM computing surveys (CSUR)*, 49(4):1–33.
- Newman, M. E. (2001). Clustering and preferential attachment in growing networks. *Physical review E*, 64(2):025102.

- Nowicki, K. and Snijders, T. A. B. (2001). Estimation and prediction for stochastic blockstructures. *Journal of the American statistical association*, 96(455):1077–1087.
- Olmos, L., Tadeo, M., Vlachogiannis, D., Alhasoun, F., Alegre, X., Ochoa, C. and Gonzalez, M. (2020). A data science framework for planning the growth of bicycle infrastructures. *Transportation Research Part C: Emerging Technologies*, 115 (in press).
- Polson, N. G., Scott, J. G., and Windle, J. (2013). Bayesian inference for logistic models using pólya-gamma latent variables. *Journal of the American statistical Association*, 108(504):1339–1349.
- Rasmussen, C. E. and Williams, C. K. (2006). *Gaussian processes for machine learning*. MIT press Cambridge, MA.
- Rodríguez-Déniz, H., Suau-Sanchez, P., and Voltes-Dorta, A. (2013). Classifying airports according to their hub dimensions: an application to the us domestic network. *Journal of Transport Geography*, 33:188–195.
- Soyk, C., Ringbeck, J. and Spinler, S. (2018). Revenue characteristics of long-haul low cost carriers (LCCs) and differences to full-service network carriers (FSNCs). *Transportation Research Part E: Logistics and Transportation Review*, 112:47–65.
- Stanley, N., Shai, S., Taylor, D., and Mucha, P. J. (2016). Clustering network layers with the strata multilayer stochastic block model. *IEEE transactions on network science and engineering*, 3(2):95–105.
- Tian, Z., Zhou, J., Szeto, W. Y., Tian, L. and Zhang, W. (2020). The rebalancing of bike-sharing system under flow-type task window. *Transportation Research Part C: Emerging Technologies*, 112:1–27.
- UNCTAD (2017). *Review of Maritime Transport 2017*. United Nations Conference on Trade and Development.
- Vlahogianni, E. I., Karlaftis, M. G., and Golias, J. C. (2014). Short-term traffic forecasting: Where we are and where we are going. *Transportation Research Part C: Emerging Technologies*, 43:3–19.
- Wang, J., Mo, H., and Wang, F. (2014). Evolution of air transport network of china 1930–2012. *Journal of Transport Geography*, 40:145–158.
- Wang, H., Zhang, X. and Wang, S. (2016). A joint optimization model for liner container cargo assignment problem using state-augmented shipping network framework. *Transportation Research Part C: Emerging Technologies*, 68:425–446.
- Watts, D. J. and Strogatz, S. H. (1998). Collective dynamics of small-world networks. *Nature*, 393(6684):440.
- Windle, J., Polson, N. G., and Scott, J. G. (2014). Sampling polya-gamma random variates: alternate and approximate techniques. *arXiv preprint arXiv:1405.0506*.
- WTTC (2018). *Travel and Tourism Economic Impact 2018*. World Travel and Tourism Council.
- Xu, K. S. and Hero, A. O. (2014). Dynamic stochastic blockmodels for time-evolving social networks. *IEEE Journal of Selected Topics in Signal Processing*, 8(4):552–562.
- Yap, M., Luo, D., Cats, O., van Oort, N. and Hoogendoorn, S. (2019). Where shall we sync? Clustering passenger flows to identify urban public transport hubs and their key synchronization priorities. *Transportation Research Part C: Emerging Technologies*, 98:433–448.
- Yildirimoglu, M. and Kim, J. (2018). Identification of communities in urban mobility networks using multi-layer graphs of network traffic. *Transportation Research Part C: Emerging Technologies*, 89:254–267.
- Zhang, D., Cao, J., Feygin, S., Tang, D., Shen, Z. and Pozdnoukhov, A. (2019). Connected population synthesis for transportation simulation. *Transportation Research Part C: Emerging Technologies*, 103:1–16.
- Zhou, T., Lü, L. and Zhang, Y.C. (2009). Predicting missing links via local information. *The European Physical Journal B*, 71(4):623–630.
- Zhou, M., Li, L., Dunson, D., and Carin, L. (2012). Lognormal and gamma mixed negative binomial regression. In *Proceedings of the International Conference on Machine Learning*, volume 2012, page 1343. NIH Public Access.

Appendix A. Normal Approximation of the Pólya-Gamma variables

The moment generating function (Polson et al., 2013) is defined as

$$m_\omega(t) = \int_0^\infty e^{t\omega} p(\omega|b, c) d\omega = \cosh^b\left(\frac{c}{2}\right) \cosh^{-b}\left(\sqrt{\frac{c^2/2-t}{2}}\right) \quad (\text{A.1})$$

Mean and variance can be readily obtained through the first two moments

$$m'_\omega(t) = \frac{b}{2\sqrt{2}} \cosh^b\left(\frac{c}{2}\right) \cosh^{-b-1}\left(\sqrt{\frac{c^2/2-t}{2}}\right) \sinh\left(\sqrt{\frac{c^2/2-t}{2}}\right) \left(\frac{c^2-2t}{2}\right)^{-1/2} \quad (\text{A.2})$$

$$m'_\omega(0) = \frac{b}{2c} \cosh^{-1}\left(\frac{c}{2}\right) \sinh\left(\frac{c}{2}\right) \quad (\text{A.3})$$

$$\mathbb{E}[\omega] = m'_\omega(0) = \frac{b}{2c} \alpha \quad (\text{A.4})$$

$$\alpha = \tanh\left(\frac{c}{2}\right) = \frac{e^c - 1}{e^c + 1} \quad (\text{A.5})$$

$$m''_\omega(t) = \left[\frac{b}{2\sqrt{2}} \cosh^b\left(\frac{c}{2}\right) \right] \left[(-b-1) \cosh^{-b-2}\left(\sqrt{\frac{c^2/2-t}{2}}\right) \sinh^2\left(\sqrt{\frac{c^2/2-t}{2}}\right) \right] \quad (\text{A.6a})$$

$$\times \frac{-1}{2\sqrt{2}} \left(\frac{c^2-2t}{2}\right)^{-1} + \frac{-1}{2\sqrt{2}} \left(\frac{c^2-2t}{2}\right)^{-1} \cosh^{-b}\left(\sqrt{\frac{c^2/2-t}{2}}\right) \quad (\text{A.6b})$$

$$+ \frac{1}{2} \left(\frac{c^2-2t}{2}\right)^{-3/2} \cosh^{-b-1}\left(\sqrt{\frac{c^2/2-t}{2}}\right) \sinh\left(\sqrt{\frac{c^2/2-t}{2}}\right) \quad (\text{A.6c})$$

$$m''_\omega(0) = \frac{b}{2\sqrt{2}} \left[\frac{b+1}{2\sqrt{2}} \left(\frac{c^2}{2}\right)^{-1} \underbrace{\cosh^{-2}\left(\frac{c}{2}\right) \sinh^2\left(\frac{c}{2}\right)}_{\alpha^2} + \frac{-1}{2\sqrt{2}} \left(\frac{c^2}{2}\right)^{-1} \right] \quad (\text{A.7a})$$

$$+ \frac{1}{2} \left(\frac{c^2}{2}\right)^{-3/2} \underbrace{\cosh^{-1}\left(\frac{c}{2}\right) \sinh\left(\frac{c}{2}\right)}_{\alpha} \quad (\text{A.7b})$$

$$\mathbb{E}[\omega^2] = m''_\omega(0) = \frac{(b^2+b)\alpha^2 - b}{4c^2} + \frac{b\alpha}{2c^3} \quad (\text{A.8})$$

$$\text{Var}[\omega] = \mathbb{E}[\omega^2] - \mathbb{E}^2[\omega] = \frac{b(\alpha^2 - 1)}{4c^2} + \frac{b\alpha}{2c^3} \quad (\text{A.9})$$

Figure A.15 present several Pólya-Gamma distributions with large shape parameter b , and their moment-matching Normal approximation using (A.4, A.9). For very large b and/or c computations should be performed in logarithmic scale to avoid numerical overflow.

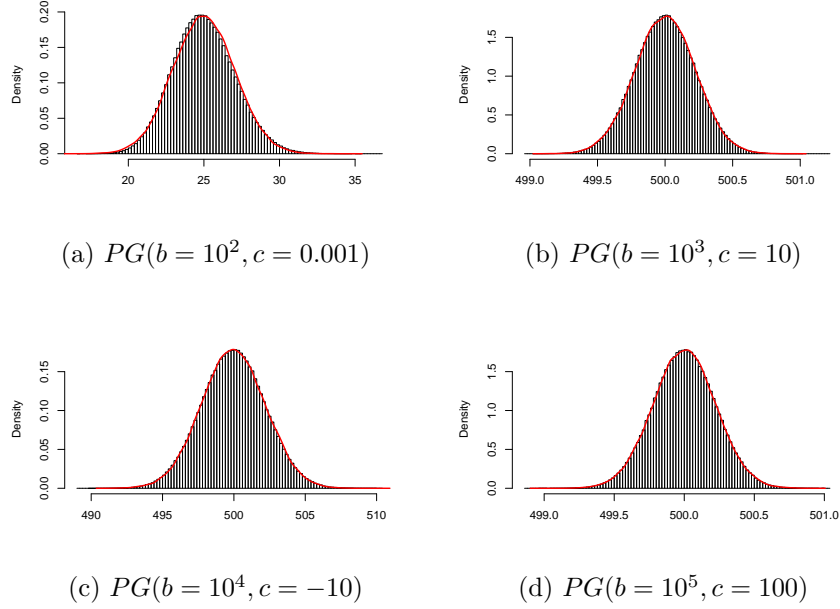


Figure A.15: Four Pólya-Gamma distributions (histograms), and their Normal approximations (red lines). Sample size is 10^6 .

Appendix B. Gibbs Sampler

Appendix B.1. Pólya-Gamma data augmentation

The proposed Gibbs sampler involves the Pólya-Gamma data augmentation trick in Polson et al. (2013). A random variable $\omega \in \mathbb{R}^+$ is said to have a Pólya-Gamma distribution, $\omega \sim PG(b, c)$ with parameters $b \in \mathbb{R}^+$ and $c \in \mathbb{R}$, if

$$\omega \stackrel{D}{=} \frac{1}{2\pi^2} \sum_{k=1}^{\infty} \frac{g_k}{(k-1/2)^2 + c^2/(4\pi^2)}, \quad g_k \stackrel{\text{iid}}{\sim} \text{Gamma}(b, 1), \quad (\text{B.1})$$

with density

$$p(\omega|b, c) = \cosh^b(c/2) \frac{2^{b-1}}{\Gamma(b)} \sum_{n=0}^{\infty} (-1)^n \frac{\Gamma(n+b)}{\Gamma(n+1)} \frac{2n+b}{\sqrt{2\pi\omega^3}} e^{-\frac{(2n+b)^2}{8\omega} - \frac{c^2\omega}{2}}. \quad (\text{B.2})$$

The relation between a Binomial likelihood and the Pólya-Gamma distribution is given the following two key results in Polson et al. (2013)

$$\frac{(e^\psi)^a}{(1+e^\psi)^b} = 2^{-b} e^{\kappa\psi} \int_0^\infty e^{-\omega\psi^2/2} p(\omega|b, 0) d\omega, \quad (\text{B.3})$$

$$p(\omega|\psi) = \frac{e^{-\omega\psi^2/2} p(\omega|b, 0)}{\int_0^\infty e^{-\omega\psi^2/2} p(\omega|b, 0) d\omega} \sim PG(b, \psi). \quad (\text{B.4})$$

To see the connection to the binomial model, note that the contribution to the likelihood of each observation in the model $y_i \sim \text{Binomial}(n_i, \pi_i)$ with $\psi_i = \text{logit}(\pi_i) = \mathbf{x}_i^T \boldsymbol{\beta}$ is

$$p(y_i|\boldsymbol{\beta}, x_i) = \frac{\exp(\mathbf{x}_i^T \boldsymbol{\beta})^{y_i}}{[1 + \exp(\mathbf{x}_i^T \boldsymbol{\beta})]^{n_i}}. \quad (\text{B.5})$$

Using Eq. (B.3) this can be expressed as

$$p(y_i|\boldsymbol{\beta}, x_i) \propto \exp(\kappa_i \mathbf{x}_i^T \boldsymbol{\beta}) \int_0^\infty \exp(-\omega_i (\mathbf{x}_i^T \boldsymbol{\beta})^2 / 2) p(\omega_i | n_i, 0) \quad (\text{B.6})$$

where $\kappa_i = y_i - n_i/2$ and $\omega_i \sim PG(n_i, 0)$. By conditioning on the Pólya-Gamma variables $\boldsymbol{\omega} = \omega_1, \dots, \omega_N$ using Eq. (B.4), direct application of Bayes' theorem yield the posterior for $\boldsymbol{\beta}$,

$$p(\boldsymbol{\beta} | \boldsymbol{\omega}, \mathbf{y}, X) \propto p(\boldsymbol{\beta}) \prod_{i=1}^N p(y_i | \boldsymbol{\beta}, \omega_i, x_i) = p(\boldsymbol{\beta}) \prod_{i=1}^N \exp(\kappa_i \mathbf{x}_i^T \boldsymbol{\beta} - \omega_i (\mathbf{x}_i^T \boldsymbol{\beta})^2 / 2) \quad (\text{B.7})$$

$$\propto p(\boldsymbol{\beta}) \exp\left(-\frac{1}{2} (\mathbf{z} - X\boldsymbol{\beta})^T \Omega (\mathbf{z} - X\boldsymbol{\beta})\right), \quad (\text{B.8})$$

which is the posterior for a Gaussian linear regression with response \mathbf{z} , mean $X\boldsymbol{\beta}$ and known covariance matrix Ω^{-1} , where $\mathbf{z} = (\kappa_1/\omega_1, \dots, \kappa_N/\omega_N)$ and $\Omega = \text{diag}(\boldsymbol{\omega})$. Using the prior $\boldsymbol{\beta} \sim \mathcal{N}(\boldsymbol{\mu}_0, \Sigma_0)$, the Pólya-Gamma method for the Binomial model therefore results in a two-step Gibbs sampler that alternates between

$$\omega_i | \boldsymbol{\beta}, X \sim PG(n_i, \mathbf{x}_i^T \boldsymbol{\beta}) \quad (\text{B.9a})$$

$$\boldsymbol{\beta} | X, \mathbf{y}, \boldsymbol{\omega} \sim \mathcal{N}(\boldsymbol{\mu}_\omega, \Sigma_\omega) \quad (\text{B.9b})$$

where

$$\boldsymbol{\mu}_\omega = \Sigma_\omega (X^T \boldsymbol{\kappa} + \Sigma_0^{-1} \boldsymbol{\mu}_0) \quad (\text{B.10a})$$

$$\Sigma_\omega = (X^T \Omega X + \Sigma_0^{-1})^{-1}. \quad (\text{B.10b})$$

Appendix B.2. Updating steps

1. Update the block probabilities

Compute the clustering quantities given the current assignments z

$$n_p = \sum_{i=1}^N \mathbb{I}(z_i = p), \text{ for all } p = 1, \dots, B$$

$$n_{pq}^k(t) = n_p n_q - n_p \mathbb{I}(p = q), \text{ for all } \{p, q\} \in \{1, \dots, B\}, t = t_1, \dots, t_T, k = 1, \dots, K$$

$$y_{pq}^k(t) = \sum_{\{i,j\}: z_i=p, z_j=q} A_{ij}^k(t), \text{ for all } \{p, q\} \in \{1, \dots, B\}, t = t_1, \dots, t_T, k = 1, \dots, K$$

Sample the vector of block probabilities η_1, \dots, η_B

$$\eta | - \sim \text{Dirichlet}(\alpha_1 + n_1, \dots, \alpha_B + n_B)$$

2. Generate the Pólya-Gamma variables

Sample the augmented data $\omega_{pq}^k(t)$

for each time $t = t_1, \dots, t_T$, layer $k = 1, \dots, K$ and block pair $\{p, q\} \in \{1, \dots, B\}$ **do**

if $p = q$ **then** $c = \mu_p^k(t) + \sum_{r=1}^R \bar{x}_{pr}(t)$ **else** $c = \mu(t) + \bar{x}_p^T(t) \bar{x}_q(t) + x_p^{kT}(t) x_q^k(t)$

Let $b = n_{pq}^k(t)$ and $\alpha = \tanh(0.5c)$

if $b < 100$ **then** $\omega_{pq}^k(t) | - \sim PG(b, c)$ **else** $\omega_{pq}^k(t) | - \sim \mathcal{N}\left(\frac{b}{2c} \alpha, \frac{b(\alpha^2 - 1)}{4c^2} + \frac{b\alpha}{2c^3}\right)$

end for

3. Update the between-block dynamic mean

Sample the vector $\boldsymbol{\mu}(t) = [\mu(t_1), \dots, \mu(t_T)]^T$ from

$$\boldsymbol{\mu} | - \sim \mathcal{N}_T(\boldsymbol{\mu}_\mu, \Sigma_\mu)$$

$$\Sigma_\mu = \left[\text{diag} \left\{ \sum_{k=1}^K \sum_{p=2}^B \sum_{q=1}^{p-1} \omega_{pq}^k(t_1), \dots, \sum_{k=1}^K \sum_{p=2}^B \sum_{q=1}^{p-1} \omega_{pq}^k(t_T) \right\} + K_\mu^{-1} \right]$$

$$\boldsymbol{\mu}_\mu = \Sigma_\mu^{-1} \begin{bmatrix} \sum_{k=1}^K \sum_{p=2}^B \sum_{q=1}^{p-1} \{y_{pq}^k(t_1) - n_{pq}^k(t_1)/2 - \omega_{pq}^k(t_1) [\bar{x}_p^T(t_1) \bar{x}_q(t_1) + x_p^{kT}(t_1) x_q^k(t_1)]\} \\ \vdots \\ \sum_{k=1}^K \sum_{p=2}^B \sum_{q=1}^{p-1} \{y_{pq}^k(t_T) - n_{pq}^k(t_T)/2 - \omega_{pq}^k(t_T) [\bar{x}_p^T(t_T) \bar{x}_q(t_T) + x_p^{kT}(t_T) x_q^k(t_T)]\} \end{bmatrix}$$

4. Update the cross-layer block coordinates

Sample the vectors $\bar{x}_p(t_1), \dots, \bar{x}_p(t_T)$ for every block and layer

for each block $p = 1, \dots, B$ **do**

Block-sample $\{\bar{x}_p(t_1), \dots, \bar{x}_p(t_T)\}$ conditioned on $\{\bar{x}_q(t) : p \neq q, t = t_1, \dots, t_T\}$

Let $\bar{x}_p = \{\bar{x}_{p1}(t_1), \dots, \bar{x}_{p1}(t_T), \dots, \bar{x}_{pR}(t_1), \dots, \bar{x}_{pR}(t_T)\}$

Let $x_p^k = \{x_{p1}^k(t_1), \dots, x_{p1}^k(t_T), \dots, x_{pH}^k(t_1), \dots, x_{pH}^k(t_T)\}$

for each layer $k = 1, \dots, K$ and $q < p$ **do**

Define a Bayesian logistic regression with \bar{x}_p as coefficient vector like

$$y_p^k \sim \text{Binomial}(n_p^k, \pi_p^k), \quad \text{logit}(\pi_p^k) = \tilde{\mu} + \bar{X}_{-p} \bar{x}_p + X_{-p}^k x_p^k$$

$$y_p^k = \left[\bigcup_{p \neq q} \{y_{pq}^k(t_1), \dots, y_{pq}^k(t_T)\}, \{y_{pp}^k(t_1), \dots, y_{pp}^k(t_T)\} \right]^\top$$

$$n_p^k = \left[\bigcup_{p \neq q} \{n_{pq}^k(t_1), \dots, n_{pq}^k(t_T)\}, \{n_{pp}^k(t_1), \dots, n_{pp}^k(t_T)\} \right]^\top$$

$$\pi_p^k = \left[\bigcup_{p \neq q} \{\pi_{pq}^k(t_1), \dots, \pi_{pq}^k(t_T)\}, \{\pi_{pp}^k(t_1), \dots, \pi_{pp}^k(t_T)\} \right]^\top$$

$$\tilde{\mu} = [\mathbf{1}_{B-1} \otimes \mu, \mu_p^k]^\top$$

The prior is $\bar{x}_p \sim \mathcal{N}_{T \times R}(0, \text{diag}(\tau_1^{-1}, \dots, \tau_R^{-1}) \otimes K_{\bar{x}})$. Design matrices \bar{X}_{-p} and \bar{X}_{-p}^k contain regressors chosen respectively from \bar{x}_p and x_p^k to fulfill Eq. (8).

Ω_p^k is a diagonal matrix with the corresponding Pólya-Gamma variables.

end for

Using the above specification the update of \bar{x}_p becomes

$$\bar{x}_p | - \sim \mathcal{N}_{T \times R}(\mu_{\bar{x}_p}, \Sigma_{\bar{x}_p})$$

$$\Sigma_{\bar{x}_p} = \left[\bar{X}_{-p}^\top (\sum_{k=1}^K \Omega_p^k) \bar{X}_{-p} + \text{diag}(\tau_1, \dots, \tau_R) \otimes K_{\bar{x}}^{-1} \right]$$

$$\mu_{\bar{x}_p} = \Sigma_{\bar{x}_p}^{-1} \left[\bar{X}_{-p}^\top (\sum_{k=1}^K \{y_p^k - n_p^k(t)/2 - \Omega_p^k [\tilde{\mu} + X_{-p}^k x_p^k]\}) \right]$$

end for

5. Update the within-layer coordinates

Sample the vectors $x_p^k(t_1), \dots, x_p^k(t_T)$ for every block and layer

for each layer $k = 1, \dots, K$ **do**

for each block $p = 1, \dots, B$ **do**

Block-sample $\{x_p^k(t_1), \dots, x_p^k(t_T)\}$ conditioned on $\{x_q^k(t) : p \neq q, t = t_1, \dots, t_T\}$

Adapting Step 4 to fulfill Eq. (8) yields the following update for x_p^k

$$x_p^k | - \sim \mathcal{N}_{T \times H}(\mu_{x_p^k}, \Sigma_{x_p^k})$$

$$\Sigma_{x_p^k} = \left[X_{-p}^{k\top} \Omega_p^k X_{-p}^k + \text{diag}(\tau_1^k, \dots, \tau_H^k) \otimes K_x^{-1} \right]$$

$$\mu_{x_p^k} = \Sigma_{x_p^k}^{-1} \left[X_{-p}^{k\top} (y_p^k - n_p^k(t)/2 - \Omega_p^k [\mathbf{1}_{B-1} \otimes \mu + \bar{X}_{-p} \bar{x}_p]) \right]$$

end for

end for

6. Update the cross-layer shrinkage parameters

Sample the gamma quantities that define the shrinkage parameters τ_1, \dots, τ_R

$$\delta_1 | - \sim \text{Gamma} \left(a_1 + \frac{B \times T \times R}{2}, 1 + 0.5 \sum_{m=1}^R \theta_m^{(-1)} \sum_{p=1}^B \bar{x}_{pm}^\top K_{\bar{x}}^{-1} \bar{x}_{pm} \right)$$

$$\delta_{r \geq 2} | - \sim \text{Gamma} \left(a_2 + \frac{B \times T \times (R-r+1)}{2}, 1 + 0.5 \sum_{m=r}^R \theta_m^{(-r)} \sum_{p=1}^B \bar{x}_{pm}^\top K_{\bar{x}}^{-1} \bar{x}_{pm} \right)$$

where $\theta_m^{(-r)} = \prod_{f=1, f \neq r}^m \delta_f$ for $r = 1, \dots, R$ and $\bar{x}_{pm} = \{\bar{x}_{pm}(t_1), \dots, \bar{x}_{pm}(t_T)\}^\top$

7. Update the within-layer shrinkage parameters

for each layer $k = 1, \dots, K$ **do**

Sample the gamma quantities that define the within-layer $\tau_1^k, \dots, \tau_H^k$

$$\delta_1^k | - \sim \text{Gamma} \left(a_1 + \frac{B \times T \times H}{2}, 1 + 0.5 \sum_{l=1}^H \theta_l^{(-1)} \sum_{p=1}^B x_{pl}^{k\top} K_x^{-1} x_{pl}^k \right)$$

$$\delta_{h \geq 2}^k | - \sim \text{Gamma} \left(a_2 + \frac{B \times T \times (H-h+1)}{2}, 1 + 0.5 \sum_{l=1}^H \theta_l^{(-h)} \sum_{p=1}^B x_{pl}^{k\top} K_x^{-1} x_{pl}^k \right)$$

where $\theta_l^{(-h)} = \prod_{f=1, f \neq h}^l \delta_f^k$ for $h = 1, \dots, H$ and $x_{pl}^k = \{x_{pl}^k(t_1), \dots, x_{pl}^k(t_T)\}^\top$

end for

8. Update the within-block dynamic mean

Sample the vector $\mu_p^k(t) = [\mu_p^k(t_1), \dots, \mu_p^k(t_T)]^\top$ for every block and layer

for each block $p = 1, \dots, B$ and layer $k = 1, \dots, K$ **do**

$$\mu_p^k | - \sim \mathcal{N}_T(\mu_{\mu_p}, \Sigma_{\mu_p})$$

$$\Sigma_{\mu_p} = \left[\text{diag} \{ \omega_{pp}^k(t_1), \dots, \omega_{pp}^k(t_T) \} + K_{\mu_p}^{-1} \right]$$

$$\mu_{\mu_p} = \Sigma_{\mu_p}^{-1} \begin{bmatrix} y_{pp}^k(t_1) - n_{pp}^k(t_1)/2 - \omega_{pp}^k(t_1) \sum_{r=1}^R \bar{x}_{pr}(t) \\ \vdots \\ y_{pp}^k(t_T) - n_{pp}^k(t_T)/2 - \omega_{pp}^k(t_T) \sum_{r=1}^R \bar{x}_{pr}(t) \end{bmatrix}$$

end for

9. Compute posterior block probabilities

Obtain the posterior block probabilities $\pi_{pq}^k(t)$

for each time $t = t_1, \dots, t_T$, layer $k = 1, \dots, K$ and block pair $\{p, q\} \in \{1, \dots, B\}$ **do**

if $p \neq q$ **then**

$$\pi_{pq}^k(t) = [1 + \exp\{-\mu(t) - \bar{x}_p^\top(t) \bar{x}_q(t) - x_p^{k\top}(t) x_q^k(t)\}]^{-1}$$

else

$$\pi_{pp}^k(t) = [1 + \exp\{-\mu_p^k(t) - \sum_{r=1}^R \bar{x}_{pr}(t)\}]^{-1}$$

end if

end for

10. Update the block assignments

Sample the latent block assignments z sequentially.

Denote z_i^* if the assignment of vertex i has been already updated, and z_i otherwise.

for each vertex $i = 1, \dots, N$ **do**

Let $\tilde{z} = [z_1^*, \dots, z_{i-1}^*, z_{i+1}, \dots, z_N]$

for each block $p = 1, \dots, B$ **do**

$$\gamma_{ip} = p(z_i = p | -) \propto \eta_p \prod_{t=t_1}^{t_T} \prod_{k=1}^K \prod_{q=1}^B [\pi_{pq}^k(t)]^{j \neq i: \tilde{z}_j = q} \sum_{i_j} A_{ij}^k(t) [1 - \pi_{pq}^k(t)]^{j \neq i: \tilde{z}_j = q} \sum_{i_j} 1 - A_{ij}^k(t)$$

end for

$$z_i | - \sim \text{Categorical}(\gamma_i)$$

end for

Note: The pseudocode above describes a complete update of all z_i 's though we strongly recommend random-scan Gibbs sampling to alleviate the computational burden. In a random-scan the outer loop will iterate only over the z_i 's randomly selected at a given MCMC step, and the vector \tilde{z} will not have a sequential structure but need to be defined appropriately. All other calculations remain the same.

11. [Optional] Edge prediction/imputation

Sample the unobserved edges from $\pi_{pq}^k(t^*)$.

Let $t^* \subset t$ be the unobserved time intervals, and denote the unobserved part of the data as $A_u = A_{ij}^k(t^*)$.

for each time $t^* \in \{t_1^*, \dots, t_{T^*}^*\}$, layer $k = 1, \dots, K$ and vertex pair $\{i, j\} \in \{1, \dots, N\}$ **do**
 Impute the unobserved edges from $A_u|_{-} \sim \text{Bernoulli}(\pi_{z_i z_j}^k(t^*))$
end for

Appendix C. Notation

Symbol	Meaning
$N \in \mathbb{N}$	Number of network nodes/vertices
$\{i, j\} = 1, \dots, N$	Indices for the network nodes
$T \in \mathbb{N}$	Number of time intervals
$t = t_1, \dots, t_T$	Index for the time intervals
$K \in \mathbb{N}$	Number of network layers
$k = 1, \dots, K$	Index for the network layers
$B \in \mathbb{N}$	Number of network blocks/clusters
$\{p, q\} = 1, \dots, B$	Indices for the network blocks
$A_{ij}^k(t) \in \{0, 1\}$	Adjacency matrix at time t and layer k
$\theta_{ij}^k(t) \in [0, 1]$	Matrix of edge probabilities at time t and layer k
$\pi_{pq}^k(t) \in [0, 1]$	Matrix of block probabilities at time t and layer k
$\psi_{pq}^k(t) \in \mathbb{R}^+$	Logit of the block probabilities at time t and layer k
$\bar{x}_{pr}(t) \in \mathbb{R}$	Latent between-layer coordinate r , for block p at time t
$x_{ph}^k(t) \in \mathbb{R}$	Latent within-layer coord. h , for block p , at time t and layer k
$\mu(t) \in \mathbb{R}$	Latent between-block intercept at time t
$\mu_p^k(t) \in \mathbb{R}$	Latent within-block intercept for block p , at time t and layer k
$\tau_r \in \mathbb{R}^+$	Shrinkage parameter for the latent between-layer coordinate r
$\tau_h^k \in \mathbb{R}^+$	Shrinkage for the latent within-layer coordinate h at layer k
$\delta_r \in \mathbb{R}^+$	Gamma for shrinkage parameter τ_r
$\delta_h^k \in \mathbb{R}^+$	Gamma for shrinkage parameter τ_h^k
$\{a_1, a_2\} \in \mathbb{R}^+$	Shape hyperparameters for the shrinkage Gammas
$z_i \in \{0, \dots, B\}$	Block/cluster assignment vector
$\eta_p \in [0, 1]$	Prior probability that a node belongs to block p
$\alpha = \{\alpha_1, \dots, \alpha_B\} \in [0, 1]$	Concentration hyperparameter vector for η
$\gamma_{ip} = p(z_i = p) \in [0, 1]$	Posterior probability that node i belongs to block p
$n_p \in \mathbb{N}$	Number of vertices in block p , such that $\sum_{p=1}^B n_p = N$
$n_{pq}^k(t) \in \mathbb{N}$	Matrix of potential edges b/w blocks $\{p, q\}$, at time t , layer k
$y_{pq}^k(t) \in \mathbb{N}$	Matrix of actual edges b/w blocks $\{p, q\}$, at time t , layer k
$\omega_{pq}^k(t) \in \mathbb{R}^+$	Pólya-Gamma variable for block pair $\{p, q\}$, at time t , layer k
$\Omega = \text{diag}(\omega_{pq}^k(t)) \in \mathbb{R}^+$	Matrix with diagonal Pólya-Gamma variables
$k_f(t, t') \in \mathbb{R}^+$	Kernel function for latent variable f
$l \in \mathbb{R}^+$	Lengthscale for a Radial-Basis-Function kernel
$K_f \in \mathbb{R}^+$	Gramian matrix from the kernel $k_f(t, t')$
$T^* \in \mathbb{N}$	Number of unobserved time intervals, $T^* < T$
$t^* = t_1^*, \dots, t_{T^*}^*$	Index for the unobserved time intervals, $t^* \subset t$
$A_u = A_{ij}^k(t^*)$	Unobserved adjacency matrices
$D^k(t)$	Network density at time t and layer k
$d_i^k(t)$	Degree of the vertex i at time t and layer k
$S_{ij}^k(t)$	Matrix of smoothed similarity scores at time t and layer k

Appendix D. IATA Airport Codes

IATA	Airport	IATA	Airport
ABQ	Albuquerque Intl.	MCO	Orlando Intl.
ALB	Albany Intl.	MDW	Chicago Midway Intl.
ATL	Hartsfield-Jackson Atlanta Intl.	MEM	Memphis Intl.
AUS	Austin Bergstrom Intl.	MHT	Manchester-Boston Regional
BDL	Hartford Bradley Intl.	MIA	Miami Intl.
BHM	Birmingham-Shuttlesworth Intl.	MKE	Milwaukee General Mitchell Intl.
BNA	Nashville Intl.	MSP	Minneapolis-St Paul Intl.
BOI	Boise Air Terminal	MSY	Louis Armstrong New Orleans Intl.
BOS	Boston Logan Intl.	OAK	Metropolitan Oakland Intl.
BUF	Buffalo Niagara Intl.	OGG	Kahului Airport
BUR	Burbank Bob Hope	OKC	Oklahoma City
BWI	Baltimore/Washington Intl.	OMA	Omaha Eppley Airfield
CHS	Charleston AFB/Intl.	ONT	Ontario Intl.
CLE	Cleveland-Hopkins Intl.	ORD	Chicago O'Hare Intl.
CLT	Charlotte Douglas Intl.	ORF	Norfolk Intl.
CMH	John Glenn Columbus Intl.	PBI	Palm Beach Intl.
CVG	Cincinnati/Northern Kentucky Intl.	PDX	Portland Intl.
DAL	Dallas Love Field	PHL	Philadelphia Intl.
DCA	Ronald Reagan Washington National	PHX	Phoenix Sky Harbor Intl.
DEN	Denver Intl.	PIT	Pittsburgh Intl.
DFW	Dallas/Fort Worth Intl.	PNS	Pensacola Intl.
DTW	Detroit Metro Wayne County	PVD	Providence Theodore Francis Green
ELP	El Paso Intl.	RDU	Raleigh-Durham Intl.
EWR	Newark Liberty Intl.	RIC	Richmond, VA: Richmond Intl.
FLL	Fort Lauderdale-Hollywood Intl.	RNO	Reno/Tahoe Intl.
GEG	Spokane Intl.	RSW	Fort Myers Southwest Florida Intl.
GRR	Grand Rapids Gerald R. Ford Intl.	SAN	San Diego Intl.
HNL	Honolulu Intl.	SAT	San Antonio Intl.
HOU	Houston William P Hobby	SAV	Savannah/Hilton Head Intl.
IAD	Washington Dulles Intl.	SDF	Louisville Intl.-Standiford Field
IAH	Houston George Bush Intl.	SEA	Seattle/Tacoma Intl.
IND	Indianapolis Intl.	SFO	San Francisco Intl.
ISP	Long Island MacArthur	SJC	Norman Y. Mineta San Jose Intl.
JAX	Jacksonville Intl.	SLC	Salt Lake City Intl.
JFK	New York John F. Kennedy Intl.	SMF	Sacramento Intl.
LAS	Las Vegas McCarran Intl.	SNA	John Wayne Orange County
LAX	Los Angeles Intl.	STL	St Louis Lambert Intl.
LGA	New York La Guardia	TPA	Tampa Intl.
LIT	Little Rock Clinton Nat. Adams Field	TUL	Tulsa Intl.
MCI	Kansas City Intl.	TUS	Tucson Intl.